

Numerical and Experimental Study on the Hot Cross Wedge Rolling of Ti-6Al-4V Vehicle Lower Arm Preform

Peiai Li

University of Science and Technology Beijing

Baoyu Wang (✉ bywang@ustb.edu.cn)

University of Science and Technology Beijing

Pengni Feng

University of Science and Technology Beijing

Jinxia Shen

University of Science and Technology Beijing

Jiapeng Wang

University of Science and Technology Beijing

Research Article

Keywords: Cross wedge rolling, TC4 alloy, Microstructure evolution, Mechanical properties, Lower arm preform

Posted Date: April 8th, 2021

DOI: <https://doi.org/10.21203/rs.3.rs-384971/v1>

License:  This work is licensed under a Creative Commons Attribution 4.0 International License.

[Read Full License](#)

Version of Record: A version of this preprint was published at The International Journal of Advanced Manufacturing Technology on October 12th, 2021. See the published version at <https://doi.org/10.1007/s00170-021-07979-3>.

Numerical and Experimental Study on the Hot Cross Wedge Rolling of Ti-6Al-4V Vehicle Lower Arm Preform

Peiai Li^a, Baoyu Wang^{a,b*}, Pengni Feng^a, Jinxia Shen^a, Jiapeng Wang^a

^a School of Mechanical Engineering, University of Science and Technology Beijing, Beijing 100083, China

^b Beijing Laboratory of Metallic Materials and Processing for Modern Transportation, Beijing 100083, China

*Corresponding author: Baoyu Wang

E-mail address: bywang@ustb.edu.cn (Baoyu Wang), beibeipepei@126.com (Peiai Li)

Tel.: +86 10 82375671

Fax.: +86 10 62332923

Postal address: No.30 Xueyuan Road, Haidian District, Beijing 100083, China

Abstract

Cross wedge rolling (CWR) has unique advantages in the production of shaft preforms with refined grains and improved mechanical properties. Considering the sensitivity of Ti-6Al-4V (TC4) alloy to heat treatment temperature, the effect of different initial deformation temperatures (IDTs) on the forming quality, mechanical properties and microstructure evolution of the TC4 alloy lower arm preforms in CWR forming were studied in this work. The flow stress curves of TC4 alloy in the two-phase region were obtained by isothermal compression experiments. The Arrhenius constitutive model was established and applied to DEFORM-3D finite element (FE) software to simulate the CWR forming process of TC4 alloy lower arm preforms. The forming quality of TC4 alloy parts was compared and analyzed by 3D FE simulation and experiment. And their mechanical properties at room temperature were tested by tensile test. The results showed that the rolled part has well forming quality (no steps and necking defects) and higher geometric dimension accuracy at the IDT 850°C. Moreover, with the increase of IDT, the radial force and torque in the rolling process decrease. In addition, there were no internal defects in the parts rolled by different IDTs, because the die gap reduces the number of alternating cycles of tensile-compressive stress in the rolled workpieces. Compared with the initial state, the microstructure was refined. When the IDT is 885 °C, the ultimate tensile strength (UTS), yield strength (YS) and elongation (EI) of the parts were 987 MPa, 924 MPa and 16.8 % respectively, which was able to ensure the mechanical performance requirements of the lower arm preform. The results provide theoretical guidance for the actual production of lower arm preform by CWR.

Key words: Cross wedge rolling, TC4 alloy, Microstructure evolution, Mechanical properties, Lower arm preform

1. Introduction

Wheeled armored vehicle plays an extremely important role in the modern battlefield, anti-terrorism, peacekeeping and other fields. The number of its equipment is also increasing according

42 to strategic needs. The lower arm is the key component of wheeled armored vehicle suspension.
43 Ti-6Al-4V (TC4) has the advantages of light weight, high strength, strong corrosion resistance, making
44 it an ideal material in the aviation industry and military industry [1-3]. As the preferred material for the
45 lower arm of wheeled armored vehicle, TC4 alloy not only contributes to reducing the weight of the
46 vehicle, but also ensures that it can meet the requirements of service life under harsh road conditions.
47 Most of the forging of lower arm preforms are produced by free forging and precision forging. Due to
48 the large forging force, the free forging process is easy to form eccentricity, bending or crack when
49 forging shaft parts. The precision forging process also has the disadvantage of expensive equipment
50 and low production efficiency [4-6]. Cross wedge rolling (CWR) is a new near-net forming process,
51 which can reduce the processing cost of shaft parts and improve their quality [7].

52 Steel products with good quality can be obtained by selecting suitable die parameters and process
53 parameters during CWR [8, 9]. It is necessary for us to further explore and research how to control the
54 surface quality and internal quality of TC4 alloy shaft parts in the rolling process. Li et al. [10]
55 investigated the effects of forming angle, the stretching angle and the area reduction on the spiral
56 groove, internal defects and necking of the rolled workpiece by large number of CWR experiments.
57 Zhou et al. [11] established a twice-stage CWR finite element model (FEM), and explained the necking
58 law in detail. Pater et al. [12-14] used the method of combining experiment with 3D FE software
59 Deform to systematically investigated various defects, temperature distribution, stress-strain
60 distribution and rolling force change of workpiece during CWR. Maraghechi et al. [15] studied the
61 central damage during CWR, and revealed the formation mechanism and development process of
62 central damage by analyzing the central stress-strain state of rolled workpiece. Lee et al. [16] used the
63 response surface method to optimize the CWR process parameters and obtained the process parameters
64 to prevent the center hole defects of rolled workpiece. In addition, Studies have shown that the use of
65 gaped die can significantly reduce the torsional deformation of the workpiece [17]. In the range of
66 small area reduction ($\psi < 55\%$), the use of gaped die was conducive to reducing the rolling force in the
67 CWR process [18]. Pater et al. [19] studied the temperature and damage distribution in the process of
68 CWR forming TC4 alloy drive shaft. The results showed that the damage factor reaches the maximum
69 at the center section of the rolled workpiece. Çakırcalı et al. [20] revealed the generation and
70 development of cracks in TC4 alloy workpiece during CWR process by FE simulation and experiments.
71 However, the study by Huang et al. [21] showed that when the hollow shaft parts with different wall
72 thicknesses were rolled by the gaped die in the CWR process, step defects with different heights
73 appeared on the outer surface of the rolled workpiece. With the increase of ellipticity of hollow parts,
74 the step defects were more obvious. He pointed out that this was caused by the elliptical deformation of
75 the rolled workpiece in the rolling process. Ji et al. [22] studied the temperature distribution, force
76 energy parameters and forming accuracy of the TC4 alloy blade preforms during the rolling process by
77 CWR. Li et al. [23] studied the effects of die parameters and initial rolling temperature on the surface
78 quality of TC4 alloy during CWR process.

79 The mechanical properties of titanium alloy are closely related to the microstructure
80 characteristics, and the evolution of its microstructure will affect the flow behavior of the material [24].
81 TC4 alloy is sensitive to hot processing parameters. Different heat treatment conditions and
82 deformation processing parameters can regulate the size, morphology and volume fraction of the phase.
83 The equiaxed microstructure with an average grain size of $1.9\mu\text{m}$ was obtained by multi-directional
84 isothermal forging (MDIF) of TC4 alloy by Zhang et al. [25], and the mechanism of grain refinement
85 was studied. The tensile strength, yield strength and elongation of the alloy after grain refinement were

86 greatly improved at room temperature and 400 °C. Zhai et al. [26] studied the effects of α phase content
 87 and morphology on the microstructure and mechanical properties of TC4 alloy during multiple heat
 88 treatment processes by experimental method. Wang et al. [27] established the
 89 rate/temperature/microstructure constitutive model of TC4, and successfully predicted the evolution
 90 law of β -phase volume fraction and grain size during the process of hot ring rolling. Li et al. [28]
 91 studied the effects of IDT, area reduction and rolling speed on the volume fraction of α phase in TC6
 92 alloy during CWR by FEM and experimental method. Therefore, it is necessary to study the
 93 corresponding law between the microstructure characteristics and mechanical properties of TC4 alloy
 94 during hot CWR.

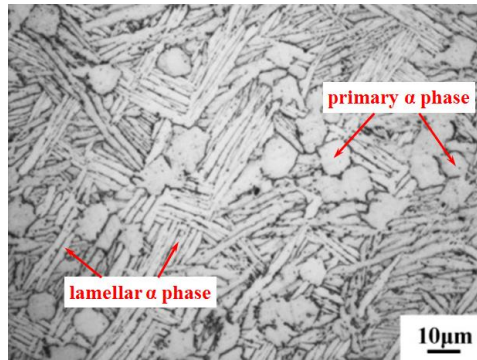
95 The hot deformation behavior of TC4 alloy with bimodal microstructure was first studied by
 96 isothermal hot compression method, and the constitutive equation of TC4 alloy was established for FE
 97 simulation. Secondly, the thermodynamic coupling numerical simulation of CWR process of TC4 alloy
 98 lower arm preform was carried out by using software Deform, and the accuracy of FEMs were verified.
 99 Thirdly, the mechanism of forming steps and slight necking on the rolled workpiece surface under
 100 different IDTs were systematically analyzed. The internal quality of the rolled workpiece was tested
 101 and analyzed. Finally, the microstructure evolution and tensile mechanical properties at room
 102 temperature of parts were compared and analyzed.

103

104 **2. TC4 alloy material characteristic**

105 **2.1 Materials and experimental procedure**

106 Figure 1 shows the microstructure of initial TC4 alloy bar. The microstructure has globular
 107 primary α phase and lamellar secondary α phase. The chemical composition of the raw material used
 108 in this experiment is shown in Table 1.



109

110 **Fig. 1** Optical micrograph of received TC4 alloy

111

112

Table 1 Chemical composition of TC4 alloy (in Wt%)

Main chemical component			Impurity content				
Ti	Al	V	Fe	C	N	H	O
Bal.	6.14	4.15	0.18	0.011	0.008	0.002	0.16

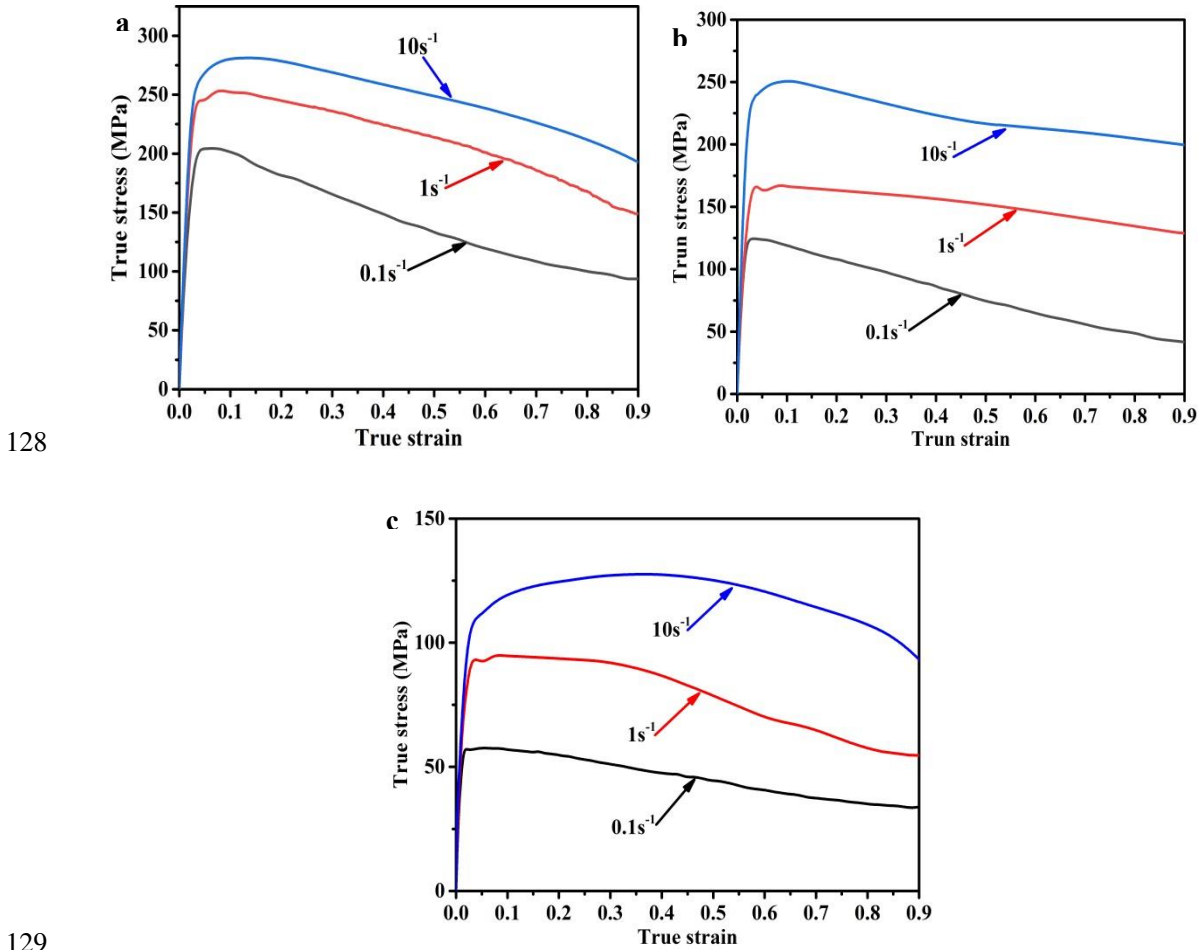
113

114 The Gleeble-1500D thermo-simulation machine was used to obtain isothermal compression data.
 115 The deformation temperatures and strain rates were set at 850°C, 900°C, 950°C, and 0.1, 1, 10 s^{-1} ,
 116 respectively. After the test, the temperature of the specimen was immediately brought down to room
 117 temperature by water cooling.

118

119 **2.2 Flow behavior**

120 The true stress-strain curves of the TC4 alloy at different strain rates and temperatures are shown
 121 in Fig. 2. The flow stress decrease with the increase of temperature, and differently, the flow stress
 122 increases with the increase of strain rate. The true stress-strain curves were all in the $\alpha+\beta$ two-phase
 123 field, and the stress increases rapidly to a peak at low strain and then decreases to the steady state,
 124 which were more prominent at higher temperatures and lower strain rates. At relatively low strain rates,
 125 dynamic recovery or dynamic recrystallization causes softening of the material flow and a significant
 126 decrease in stress value [29]. In high strain rate conditions, the flow softening and work hardening
 127 reach a balanced state, and then the flow stress-strain curve tends to be stable.



130 **Fig. 2** True stress-strain curves of TC4 alloy: **a** 850 °C, **b** 900 °C, **c** 950 °C

131 **2.3 Determination of material constants**

132 The Arrhenius equation can accurately describe the constitutive equation of TC4 alloy at high
 133 temperatures [22, 23]. The material constants can be determined separately according to the isothermal
 134 compression test data at different strain rates and temperatures. It is expressed as follows:

135
$$\dot{\epsilon} = A[\sinh(\alpha\sigma)]^n \exp\left(-\frac{Q}{RT}\right) \quad (1)$$

136 where Q ($J \cdot mol^{-1}$) is the activation energy, R is the gas constant of $8.3145 (J \cdot mol^{-1} \cdot K^{-1})$, $\dot{\epsilon}$ is the
 137 strain rate, T is the absolute temperature (K), while A , α and n are the constants.

138 The $\dot{\epsilon}$ parameters for TC4 alloy can be described by following:

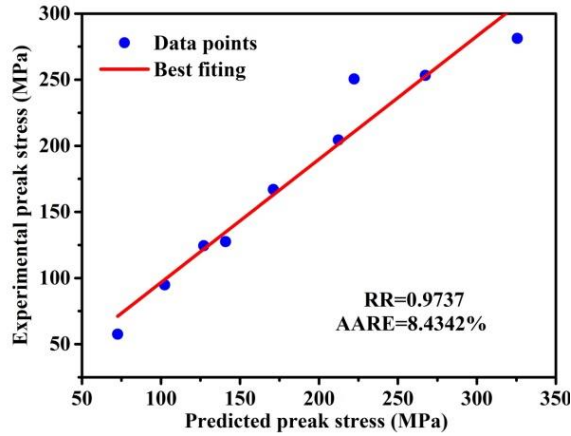
139
$$\sigma = 1.3678 \times 10^{40} [\sinh(0.0061\sigma)]^{6.1302} \exp\left(-\frac{914135}{RT}\right)$$
 (2)

140 The correlation coefficient (RR) and average absolute relative error ($AARE$) were used to evaluate
 141 the accuracy of the equation, as follows:

142
$$RR = \frac{\sum_{i=1}^N (X_i - \bar{X})(Y_i - \bar{Y})}{\sqrt{\sum_{i=1}^N (X_i - \bar{X})^2} \sqrt{\sum_{i=1}^N (Y_i - \bar{Y})^2}}$$
 (3)

143
$$AARE = \frac{1}{N} \sum_{i=1}^N \left| \frac{Y_i - X_i}{Y_i} \right| \times 100\%$$
 (4)

144 In the equations, X_i and Y_i are the predicted and experimental peak stress, \bar{X} and \bar{Y} are
 145 the average predicted and experimental peak stress, N is the number of peak stresses. Fig. 3 shows
 146 the comparison between the predicted and experimental peak stress. RR and $AARE$ are 0.9737 and
 147 8.4342%, indicating that the constitutive equation of TC4 alloy established in this paper has high
 148 credibility.



149
 150 **Fig. 3** Comparison of predicted peak stress and experimental peak stress
 151

152 **3. Finite element simulation and experiment**

153 **3.1 Finite element simulation**

154 The FEM for the CWR study is shown in Fig. 4. As the geometrical model of the test specimens
 155 and the rolling dies were symmetrical, the boundary conditions of the FEM were set to be symmetrical
 156 relative to the center plane. The following assumptions were made in the course of this study. (1)
 157 Because the deformation can be ignored, the roll dies and guide plates considered as rigid bodies. (2)
 158 The workpiece regarded as a plastic body. (3) The coefficient of friction between workpiece and tool
 159 contact surfaces was assumed to be constant. The shear friction model was used for the type of friction:
 160 $f_s = m \times k$, where f_s , k and m are the friction force, shear yield stress and the coefficient of friction,
 161 respectively. (4) The heat transfer coefficient between the workpiece and the environment, the dies are
 162 listed in detail in Table 2.

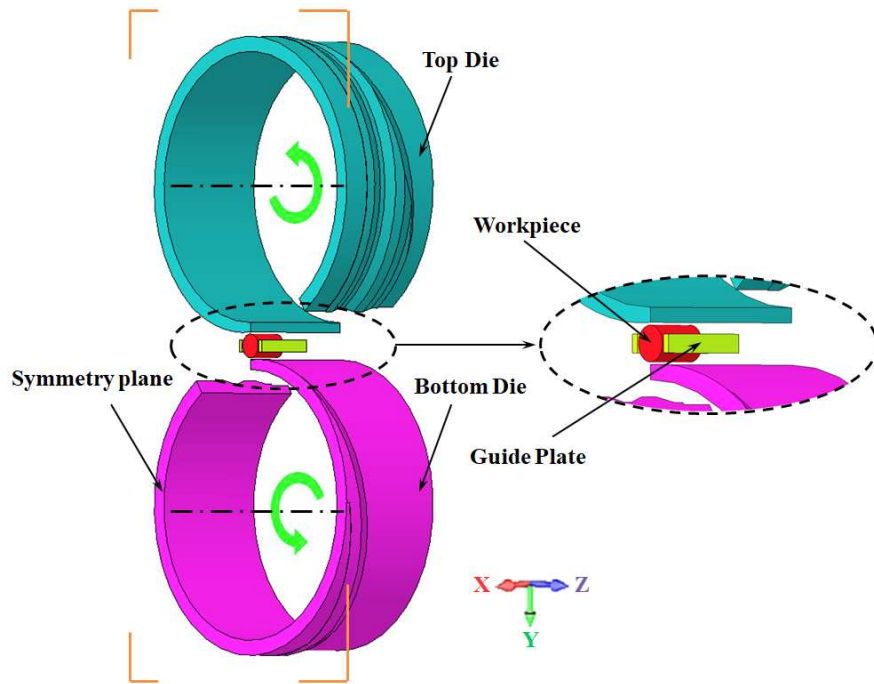


Fig. 4 FEM of CWR for TC4 alloy

163
164
165
166
167
168

The parameters of the plane layout of a CWR die are shown in Fig. 5. Only the wedge, stretching and sizing zone in the middle of the dies were used. The surface of the dies was machined with a gap of 1 mm in depth. TC4 alloy parts with an area reduction of 48%. The main technical parameters are shown in Table 2.

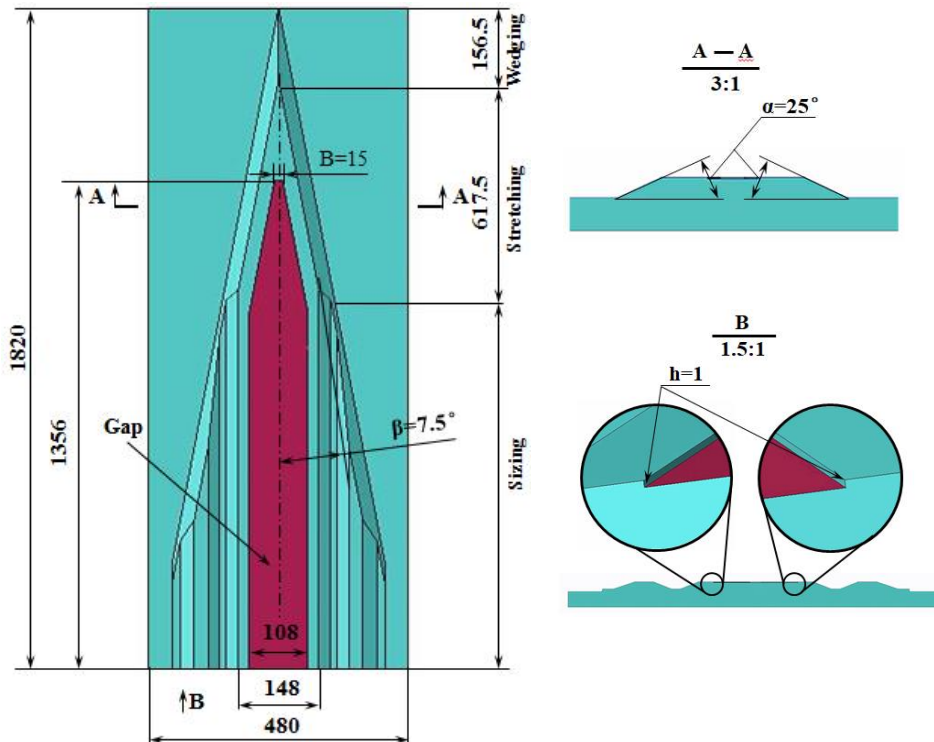


Fig. 5 Forming wedge tool parameters for H630 rolling mill

169
170
171
172
173

Table 2 Main parameters of CWR simulation

Parameters	Value
Heat transfer coefficient($Wm^{-2}K^{-1}$)	11×10^3
Convection coefficient($Wm^{-2}K^{-1}$)	20
Thermal conductivity($KWm^{-2}K^{-1}$)	17
Coefficient of mechanical energy to heating	0.9
Temperature of tools ($^{\circ}C$)	20
Friction factor between workpiece and plate	0.1
Friction factor between workpiece and die	0.9
Environment temperature ($^{\circ}C$)	20
Speed of roll (rpm)	8

175

176 3.2 Cross-wedge rolling experiment

177 The H630 CWR mill of Beijing University of Science and Technology was used for
 178 experiments. The experimental equipment is shown in Fig. 6a and the forming wedge dies are shown in
 179 Fig. 6b. Depending on the recrystallization temperature and β -phase transus temperature of TC4 alloy,
 180 four different IDTs were selected: 855 $^{\circ}C$, 885 $^{\circ}C$, 915 $^{\circ}C$ and 945 $^{\circ}C$. Before the experiment, the
 181 workpiece was heated in a tubular furnace and hold for 50 minutes. Shorten the transfer time between
 182 tube furnace and mill to reduce temperature loss. Water cooling was adopted after rolling.



183

184 **Fig. 6** Experimental equipment and manufactured die: **a** H630 mill, **b** Forming wedge dies

185 3.3 Microstructure and mechanical properties experiments

186 The parts were cut into symmetrical sections along the axial direction and in the mirror plane
 187 position respectively after rolling. The microstructure and internal quality of TC4 alloy parts were
 188 observed by cutting samples in the core of the complete forming zone.

189 The microstructure was observed by optical microscope (OM) at room temperature. Preparation of
 190 OM specimens includes mechanical grinding with sandpaper of different fineness, electrolytic
 191 polishing with 5% alcohol perchlorate solution and chemical etching with Kroll's solution. Image
 192 Pro-plus software was used to quantitatively measure the value of primary α phase. The tensile test at
 193 room temperature according to GB/T228.1-2010.

194 4. Results and discussion

195 4.1 Verification of the CWR FEM

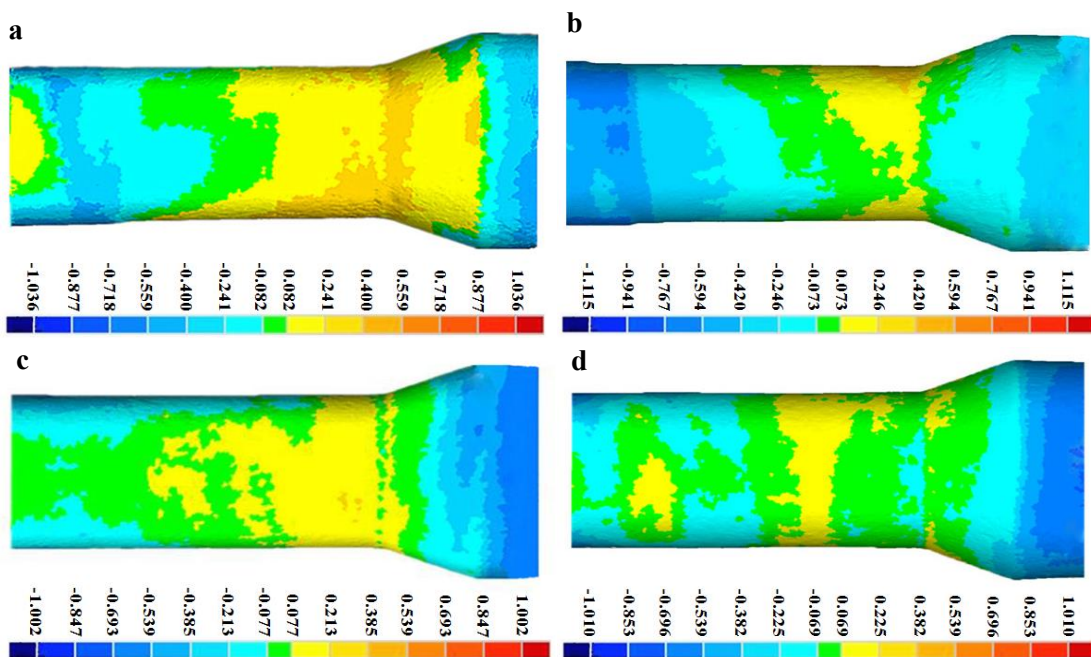
196 Figure 7 shows the appearance of TC4 alloy parts. The part at the IDT of 855 $^{\circ}C$ shows
 197 necking in the middle, while the part at 885 $^{\circ}C$ has a smooth outer surface with no folding, no

198 spiral mark and crack. However, the central of the parts at the IDT of 915 °C and 945 °C showed
 199 obvious steps and slight spiral marks.



200
 201 **Fig. 7** The parts of rolled

202 Geomagic Qualify software was used to compare the geometric dimensions of FEM and
 203 high-precision 3D scanning parts. As shown in Fig. 8a to d, the radial differences of the maximum and
 204 minimum diameters of the parts corresponding to the four simulation results are distributed in the range
 205 of 1.002 ~ 1.115 mm and -1.002 ~ -1.115 mm, respectively. The geometrical dimensions difference
 206 between the simulation results and the experimental samples is small. This shows that it is reliable to
 207 simulate the CWR forming process of TC4 alloy by FEM.

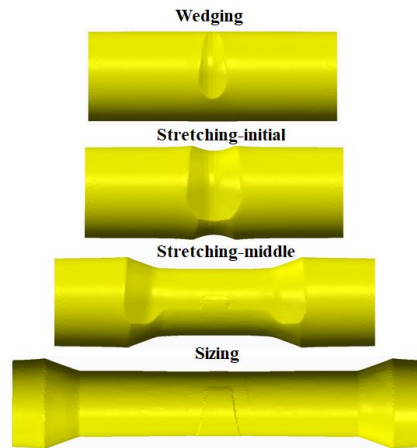


208
 209 **Fig. 8** Comparison of TC4 Alloy CWR Parts and simulated results: **a** IDT at 945°C, **b** IDT at
 210 915°C, **c** IDT at 885°C, **d** IDT at 855°C

211 4.2 Non-roundness analysis

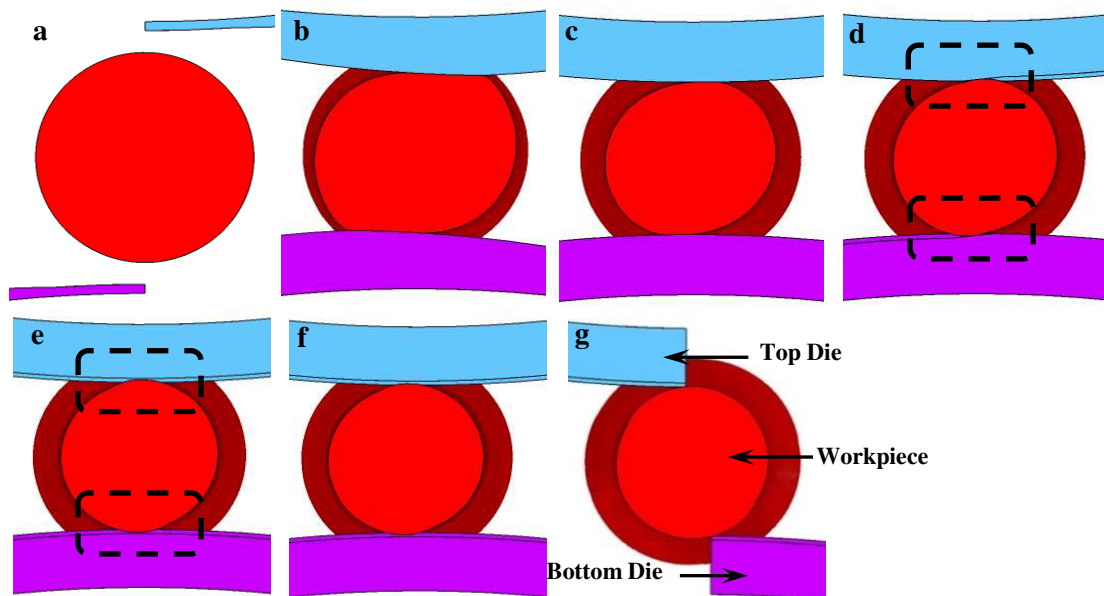
212 The CWR and step forming process of the TC4 alloy lower arm are shown in Fig. 9. When the
 213 workpieces with IDT of 915 °C and 945 °C entered the stretching zone for a short time, steps appeared
 214 on their surface. After rolling, the steps were still retained. The generation of steps not only reduces the

215 forming accuracy of the parts, but also produces defects such as folding in the follow-up forging
 216 process, causing serious harm to the performance of the lower arm, which should be avoided.

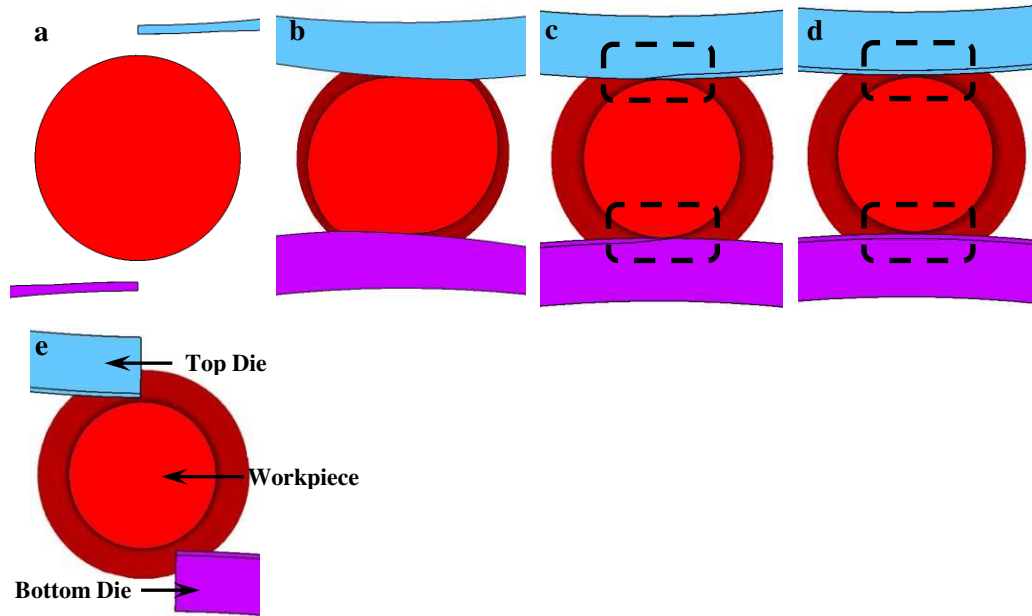


217
 218 **Fig. 9** Different stages of CWR and step forming

219 As can be seen from Fig. 10 and 11, before entering the gap area (before $t = 1.84s$), the material
 220 was gradually compressed along the axial direction by the dies. The symmetrical section of the
 221 workpiece with IDT of $945\text{ }^{\circ}\text{C}$ was still elliptical, while the symmetry section of the rolled
 222 workpiece at $880\text{ }^{\circ}\text{C}$ was circular, and the diameter was consistent with the die surface spacing.
 223 After $t = 1.84\text{ s}$, the rolled workpiece entered the gap area. The maximum diameter of the symmetrical section
 224 of the rolled workpiece with IDT of $945\text{ }^{\circ}\text{C}$ was larger than the distance between the surfaces of the top
 225 and bottom dies gap area. Therefore, the material was extruded into the cavity due to the oval
 226 deformation during rolling. The workpiece with IDT of $885\text{ }^{\circ}\text{C}$ had no material squeezed into the
 227 cavity of the gap area, and no step was formed on the surface of the rolled workpiece. The material
 228 deformation resistance is low at the high temperature, and the tangential material flow tends to increase,
 229 resulting in more serious oval deformation during rolling, which eventually leads to the formation of
 230 steps at high temperature

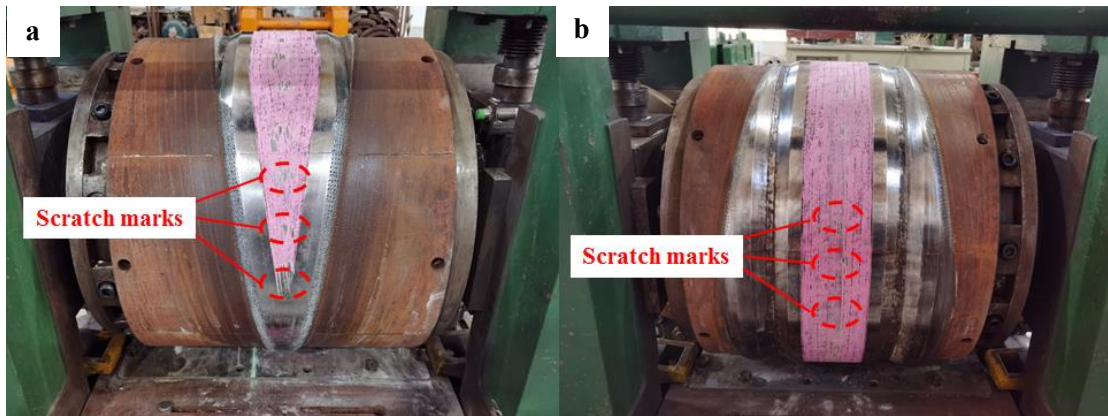


231
 232 **Fig. 10** Cross-section profile during forming process at IDT of $945\text{ }^{\circ}\text{C}$: **a** initial status $t=0s$, **b**
 233 wedging stage $t=0.8s$, **c** stretching stage $t=1.52s$, **d** preparing for the gap stage $t=1.84s$, **e** gap stage
 234 $t=2.4s$, **f** sizing stage $t=3.2s$, **g** completion status $t=5.64s$



235
236 **Fig. 11** Cross-section profile during forming process at IDT of 885 °C: **a** initial status $t=0s$, **b**
237 wedging stage $t=0.8s$, **c** preparing for the gap stage $t=1.84s$, **d** sizing stage $t=3.2s$, **e** completion
238 status $t=5.64s$

239 In Fig. 12a-b, the periodic contacts between the workpiece and the surface of die gap area
240 during rolling were recorded by smearing pink paint evenly on the surface of the die gap area.
241 This is because the rolled workpiece before entering the gap area did not form a standard circular
242 section but form an oval section with a larger size. The oval cross-section contacts with the surface
243 of the roll cavity, and the contact scratches can be recorded after rolling.



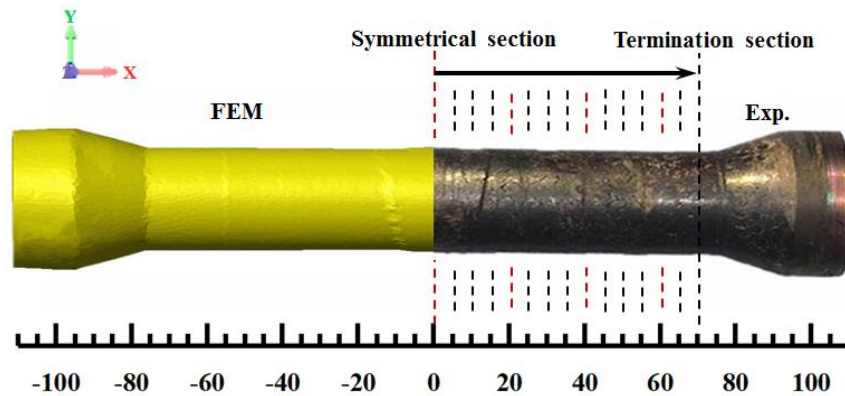
244
245 **Fig. 12** The distribution of scratch marks on the surface of the die gap area: **a** scratch marks in
246 stretching zone, **b** scratch marks in sizing zone

247 To study the variation of different cross-sectional shapes in the forming area of parts, a
248 non-circularity index should be defined [21]. The following formula (5) was used to calculate the
249 non-circularity:

$$e = \frac{2(D_{\max} - D_{\min})}{D_{\max} + D_{\min}} \quad (5)$$

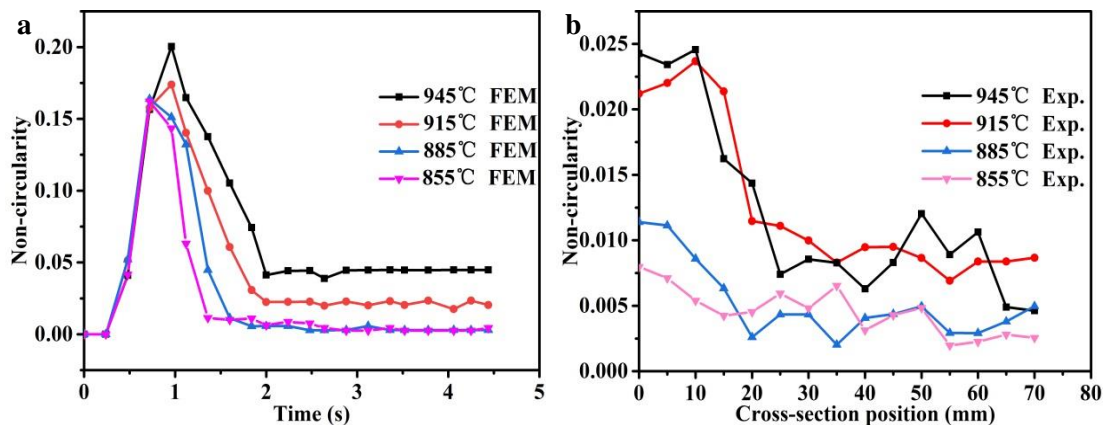
250
251 D_{\max} and D_{\min} represent the maximum diameter and minimum diameter, respectively. And e
252 represents the non-circularity.

253 In Fig. 13, the rolled workpiece of FEM with IDT of 945 °C matches well with the outer surface
 254 shape of the experiment. The projection contour curves of 15 equidistant cross-sections along the axis
 255 direction of the experimental parts were selected to analyze the dimensions of the parts after forming.



256
 257 **Fig. 13** Cross-section distribution position

258 Figure 14a shows the influence of IDT on the non-circularity of symmetrical sections. The
 259 non-circularity of the symmetrical section increases with the increase of the IDT. The lower the IDT is,
 260 the shorter the time for the non-circularity of the outer surface at the symmetrical section of the part to
 261 reach a stable value. This may be because the rolled workpiece with low IDT first reached the
 262 temperature range that is not easy to deform, which weakens the flow performance of the material. In
 263 Fig. 14b, the non-circularity value at the symmetric section position reaches the maximum, and
 264 decreases gradually along the axial direction on both sides. The reason is that at the beginning of the
 265 rolling stage, the volume of the material without deformation is relatively large. The material in the
 266 deformed zone is subjected to relatively large resistance to flow in the axial direction, which weakens
 267 the material axial flow. The material in deformation area only expands along the radial direction, so
 268 that the non-circularity is relatively large. In the subsequent rolling process, the volume of material
 269 without deformation decreases gradually, and the resistance to the flow of material along the axial
 270 direction decreases, which is relatively easy to be driven. Thus, the distribution law of the
 271 non-circularity value is obtained, which is the largest in the symmetric section and decreases gradually
 272 along the axial direction.

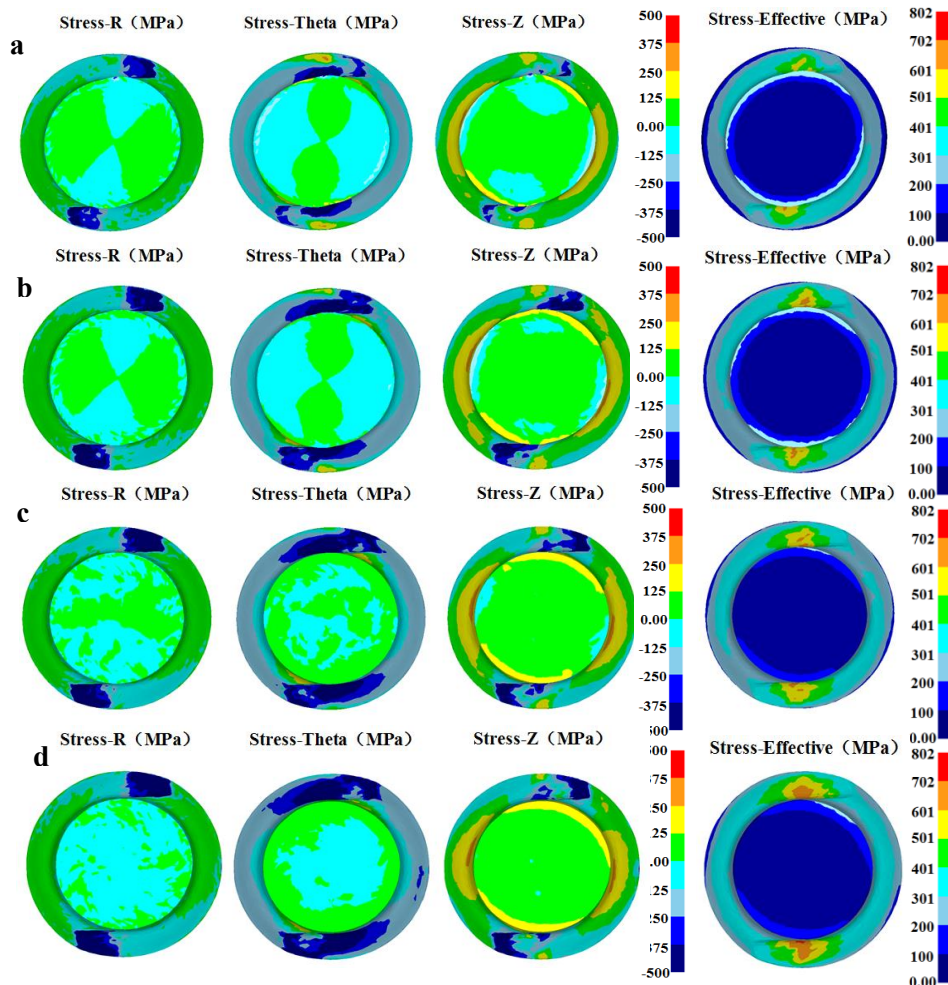


273
 274 **Fig. 14** Non-circularity value of outer surface of parts at different IDT: **a** non-circularity results of
 275 symmetric section of FEM during rolling, **b** non-circularity results of experiments at different
 276 axial position

277 4.3 Stress and strain analysis

278 This paper further analyzes the formation mechanism of non-circularity by studying the evolution

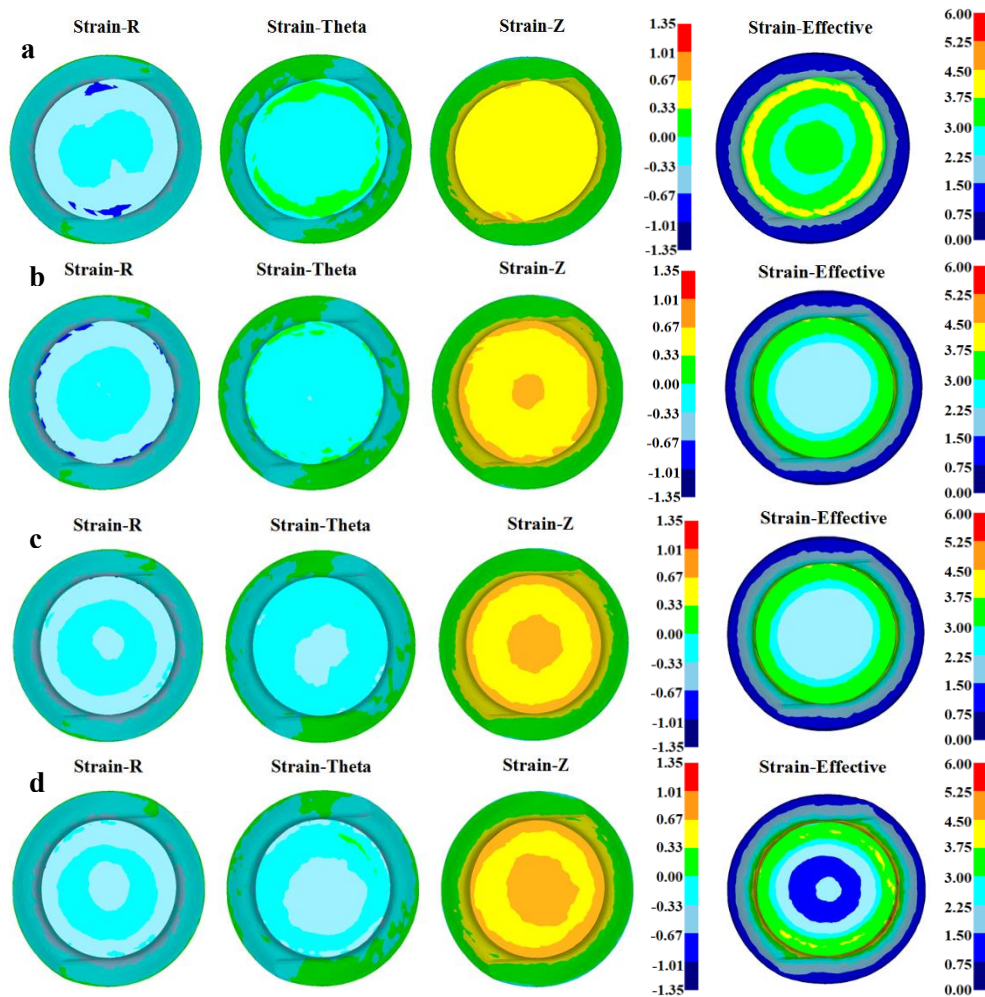
279 of stress and strain distribution of workpieces at different IDTs. Fig. 15 shows the stress distribution of
 280 the symmetrical section of the workpiece at 1.84s. Under the IDT of 945 °C and 915 °C, the
 281 symmetrical sections of the workpieces are elliptical to varying degrees. Radial stress (Stress-R) and
 282 circumferential stress (Stress-Theta) have obvious orthogonal distribution. The radial stress is
 283 tensile stress along the long-axis direction of the elliptical section and compressive stress along the
 284 short-axis direction. The distribution of circumferential stress is exactly opposite to the radial stress.
 285 With the decrease of IDT, the tensile and compressive stress distribution of radial stress tends to be
 286 uniform. The circumferential compressive stress transfers to the center of the section, and its
 287 distribution also tends to be uniform. The axial stress (Stress-Z) at the center of the cross-section at
 288 different IDTs is shown as tensile stress. In the process of IDT decreasing from 945 °C to 855 °C, the
 289 axial tensile stress range gradually expands from the central region to the outer surface. Finally, the
 290 axial stress of the section is all tensile stress.



291
 292 **Fig. 15** Stress distribution in the stretching zone: **a** T=945 °C, **b** T=915 °C, **c** T=885 °C, **d**
 293 T=855 °C

294 Figure 16 shows the strain distribution of the symmetrical section of the workpiece at 1.84s at
 295 different IDTs. The radial strain (strain-R) gradually decreases from the outer surface to the center.
 296 When the IDT at 945 °C, due to the compressive stress, the distribution of compressive strain along the
 297 long-axis in the central region is wider than that along the short-axis, and the distribution of
 298 compressive strain near the outer surface is opposite to that in the central region. It can be observed in
 299 the circumferential strain (Strain-theta) distribution that the compressive strain is all along the long-axis

300 direction, and a circular tensile strain band appears on both sides of the long-axis near the outer surface.
 301 The axial strain (Strain-Z) distribution has no significant change. The workpiece material flows to the
 302 intersection area of the long-axis and the outer surface under the combined action of the above strain,
 303 and the ovality is more obvious than other IDT conditions. As the IDT decreases, the radial strain
 304 annulus area near the outer surface gradually becomes homogeneous, and the tendency of the material
 305 flowing from the outer surface to the center tends to be the same everywhere. When the IDT decreases
 306 to 885 °C, the circumferential tensile strain gradually disappears and the circumferential compressive
 307 strain dominates the distribution. A uniform compressive strain ring is formed on the surface layer,
 308 which enables the surface material to flow uniformly along the circumferential direction, and the
 309 ovality of the section decreases. With the further decrease of IDT, the axial tensile strain value
 310 increases, the radial compressive strain region and the compressive strain value also increase, and a
 311 necking trend appears in the middle of the workpiece.

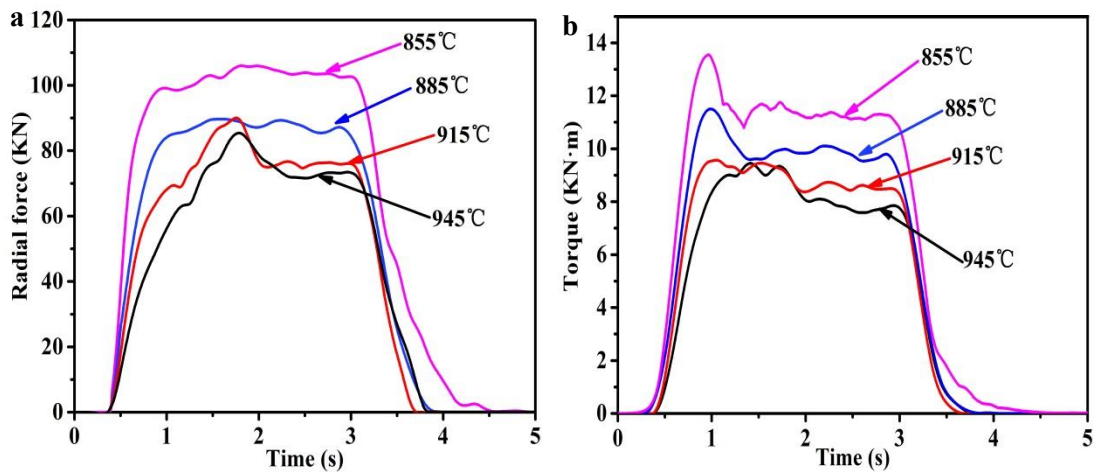


312
 313 **Fig. 16** Strain distribution in the stretching zone: **a** T= 945 °C, **b** T= 915 °C, **c** T= 885 °C, **d** T=
 314 855 °C

315 4.4 Analysis of the Force Energy Parameters

316 The force condition of the workpiece is particularly complex in the CWR process. Large plastic
 317 deformation often occurs along the axis and diameter direction of the workpiece. In order to
 318 achieve large plastic deformation, the mill needs to be able to provide sufficient rolling force and
 319 torsional moment. This is an important basis for the design of the mill and the selection of the
 320 appropriate motor power [30]. Therefore, it is essential to analyze the radial force and torque

321 corresponding to the different moments in the forming process. The radial force and torque during the
322 FE simulation of CWR are shown in full in Fig. 17.



323
324 **Fig. 17** Effective of the IDTs on force and torque in CWR processes

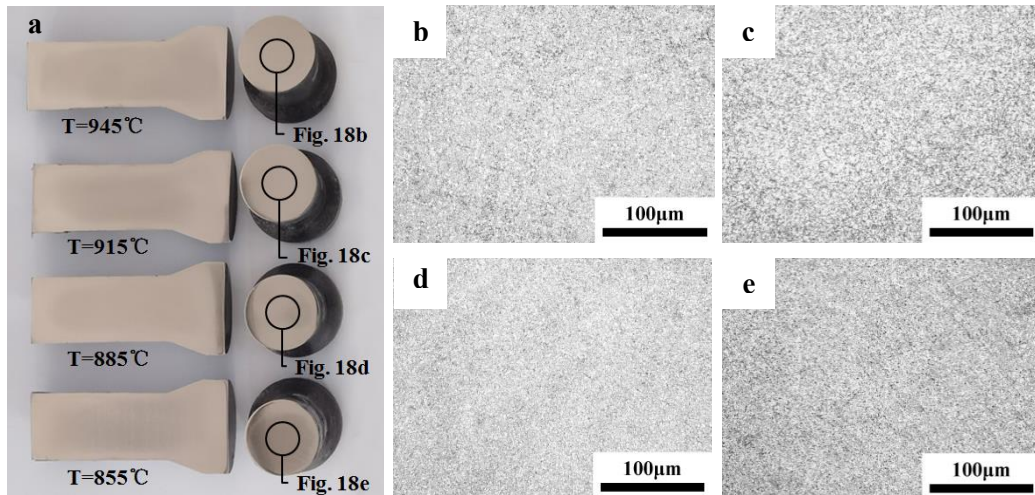
325 The steady radial force and torque gradually increase with the decrease of IDT. When the IDT is
326 945 °C, the radial force and torque are about 73 kN and 8 kN•m, respectively. When the IDT is 855 °C,
327 the radial force and torque are about 106 kN and 11.5 kN•m, respectively. The steady radial force at the
328 IDT of 855 °C increased by 45% compared with that at 945 °C, and the torque also increased by 44%.
329 This rapid increase in radial force and torque is due to the relatively high resistance to flow of TC4
330 alloy at relatively low temperature during the rolling process. When the IDT is 885 °C, the
331 non-circularity of the part keep a low level along the axial direction, and the radial force shows a
332 smooth transition during CWR process. The difference is that under the IDT conditions of 945 °C and
333 915 °C, the radial force is not uniform in the rolling cycle, and a typical elliptical peak appears at the
334 beginning of rolling, and the elliptical phenomenon occurs in both workpieces.

335 4.5 Internal quality analysis

336 In the process of plastic forming, the alternating tension-compression stress may lead to the
337 generation of cracks, and the tensile stress along the axis direction may lead to the propagation of micro
338 cracks, with cavities eventually arising as a result. The internal defects will reduce the strength of the
339 formed parts. The distribution of the stress in the stretching zone is given according to Fig. 15. During
340 the CWR process, the tensile-compression stress alternating region is formed in the symmetric center
341 of the cross-section. The stress state in this area changes four times per revolution of the workpiece.
342 The more the number of alternating cycles in the center of the workpiece, the greater the trend of
343 internal defects will occur. The stress in the CWR process increases with the decrease of IDT, which
344 means that the stress state of material is more serious in the rolling process at relatively low
345 temperature. When the IDT is high, the CWR process will make the grain boundary of the material
346 easy to form micro holes [30].

347 Figure 18 is the internal quality of samples at different IDTs. The microstructure at the central
348 position is shown in Fig. 18b to e. Compared with the specified standard GB/T5168-2008, it is difficult
349 to find any internal cave in the centre of the four parts processed at different IDTs under low and high
350 magnifications. This is mainly because the die gap reduces the interaction time between the dies and
351 the workpiece, reduces the number of alternating cycles of tension-compression stress, and prevents the
352 occurrence of central defects.

353

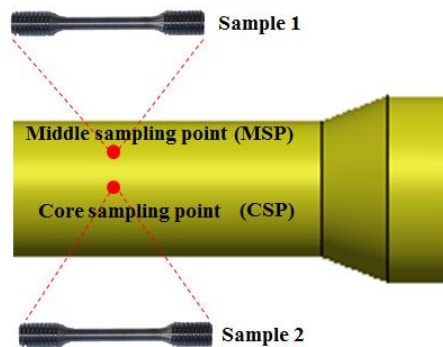


354

355 **Fig. 18** Internal quality of parts at different IDTs: **a** sectional display of different parts, **b**
 356 $T=945\text{ }^{\circ}\text{C}$, **c** $T=915\text{ }^{\circ}\text{C}$, **d** $T=885\text{ }^{\circ}\text{C}$, **e** $T=855\text{ }^{\circ}\text{C}$

357 **4.6 Mechanical properties and microstructure**

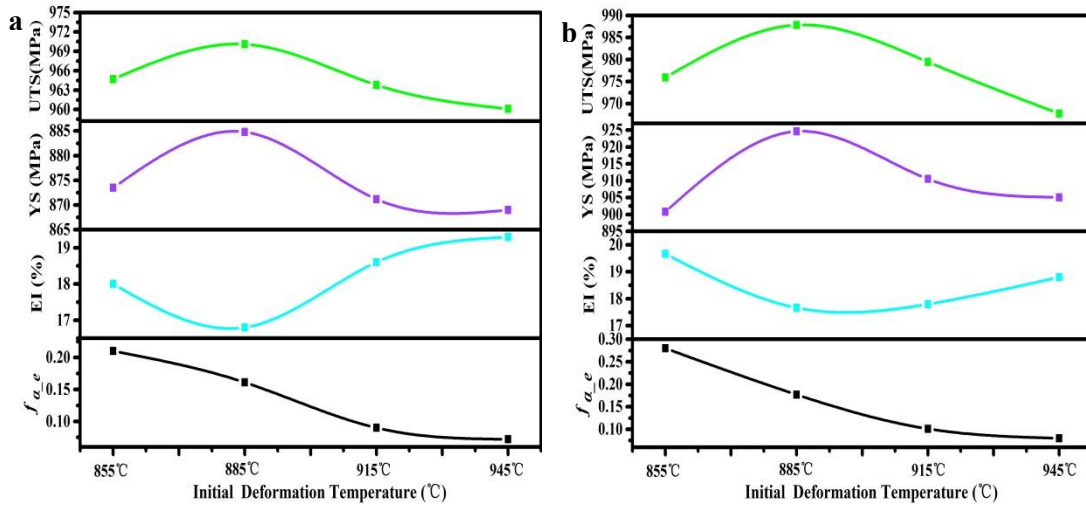
358 The mechanical properties of rolled-parts were investigated by the room temperature tensile
 359 experiment. Two tensile samples were taken along the axial direction of rolled-parts, their location is
 360 shown in Fig. 19, in which samples 1 and 2 are located in the middle and core of finished zone,
 361 respectively. The room temperature tensile strengths of the TC4 alloy in its initial state were 933 MPa,
 362 856 MPa and 19.6% for UTS, YS and EI, respectively.



363

364 **Fig. 19** Mechanical properties and microstructure test sampling position distribution

365 The room temperature mechanical properties at different IDTs are shown in Fig. 20. The UTS and
 366 YS values of rolled workpieces with different IDTs are higher than those of the initial state. It can be
 367 seen that the UTS and YS values for both core and middle samples show a tendency to increase and
 368 then decrease with increasing IDT, with the maximum value occurring at 885°C. The maximum UTS
 369 and YS values are 987 MPa and 924 MPa, respectively, which are 5.7% and 7.9% higher than those in
 370 the initial state. It has the smallest EI of 16.8%, which is 14.2% lower than the initial state.



371

372

Fig. 20 Comparison of the mechanical properties at different IDTs of **a** CSP **b** MSP

373

374

375

376

377

378

379

380

381

382

383

384

385

386

At the same IDT, the UTS and YS in the middle are higher than those in the core, this may be due to the different degrees of deformation of the microstructure along the radial direction from the surface to the center of the part. Because the effective stress and strain gradually decrease from the contact surface along the radial direction to the core position (Fig. 15 and Fig. 16), the deformation of the microstructure according to Fig. 22a-h is also decreasing. The thickness of lamellar α phase at the middle is smaller than that at the core. The α phase of the microstructure in the middle and core was refined, which improves the UTS and YS properties of the parts with different IDTs.

From the volume fraction of the equiaxed α phase (f_{α_e}) in Fig. 20a and b, the f_{α_e} decreases with the increase of IDT. Because the volume fraction of the transition from primary α phase to β phase increases with the increase of temperature [28]. The f_{α_e} at the CSP corresponding to the different IDTs are lower than that at the MSP. According to Fig. 21a and b, the plastic temperature rise level at the two points is nearly close. The MSP is close to the mold, and the temperature drop is faster than the CSP. The deformation of the MSP during rolling was larger than that of the CSP, and the lamellar α phase undergoes equiaxed transformation, which promotes the increase of the f_{α_e} .

387

388

389

390

391

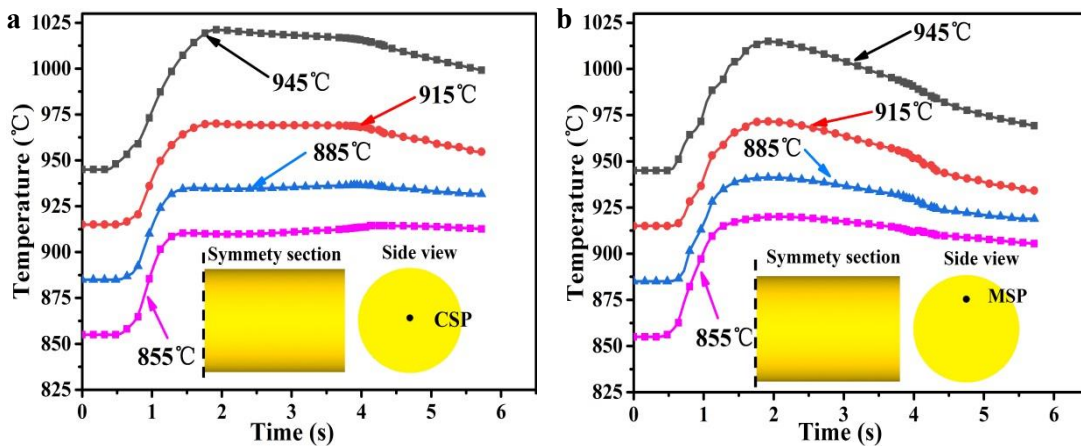
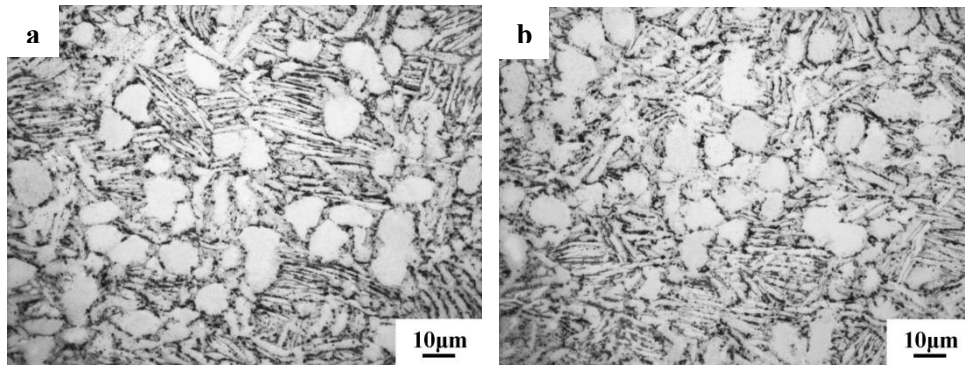


Fig. 21 Temperature distribution of CWR forming TC4 alloy in symmetry sections: **a** CSP, **b** MSP

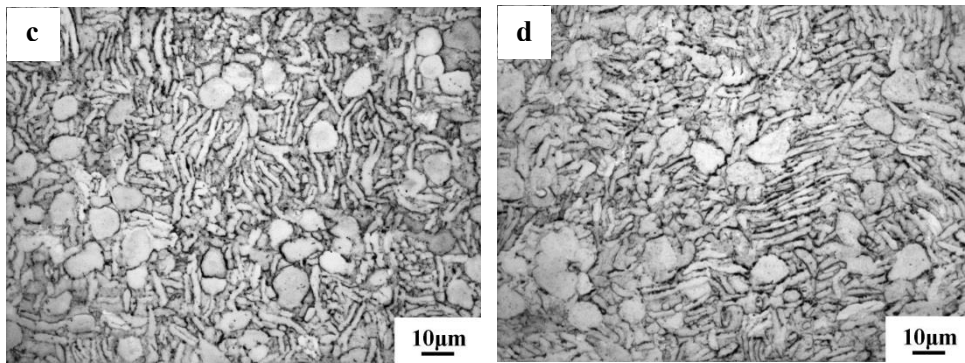
It can be seen from Fig. 22a-b and Fig. 20, when the IDT is reduced to 855 °C, the f_{α_e} value in the microstructure is the largest. With the increase of the f_{α_e} , the stability of the residual β matrix is also higher [31], which reduces the driving force for the nucleation and growth of the secondary α

392 phase, and further increases the EI value of the material and decreases the UTS and YS values. There
393 are many lamellar secondary α phases with small length-width ratio in the microstructure of Fig. 22c
394 and d. The lower length-width ratio of the secondary α phase means that the smaller the clusters with
395 the same orientation arranged between the secondary α phase and β phase, the more the corresponding
396 clusters. As a result, the crack is more likely to encounter obstacles in the process of propagation,
397 resulting in increased tensile strength of the material [26]. The secondary α phase cluster distribution in
398 the microstructure is mostly parallel to each other. The same α cluster has the same habit plane. At the
399 beginning of sliding, the coarse slip band can be formed through the parallel α cluster without
400 hindrance. Dislocation plugs are easily generated at the grain boundary of α , resulting in uneven
401 deformation in small regions. This promotes the formation and development of voids, and leads to
402 premature fracture and poor plasticity. With the increase of IDT, a large number of primary α phase and
403 lamellar secondary α phase transformed into β phase. The number of grain boundaries decrease, which
404 reduce the strength of the material. Compared with the microstructure with IDT of 885 °C, many
405 lamellar secondary α phase with large interlayer spacing appear in the microstructure of Fig. 22e to h,
406 and the thickness of lamellar secondary α phase increases and the distribution is chaotic. This makes
407 the UTS and YS of the material decreased, and the EI value increased slightly.

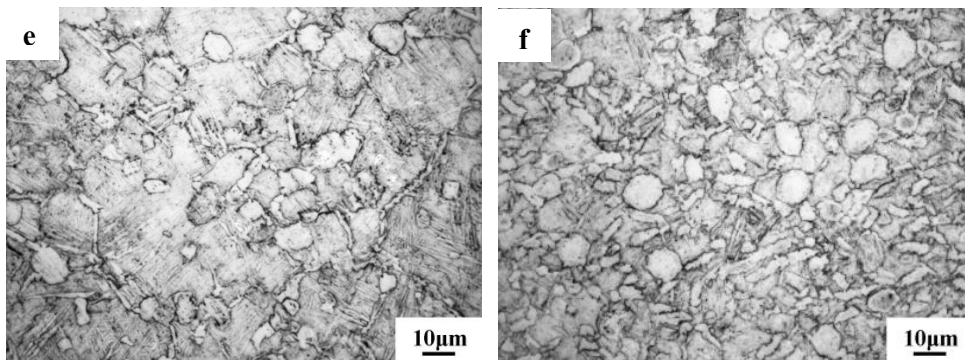
408



409



410



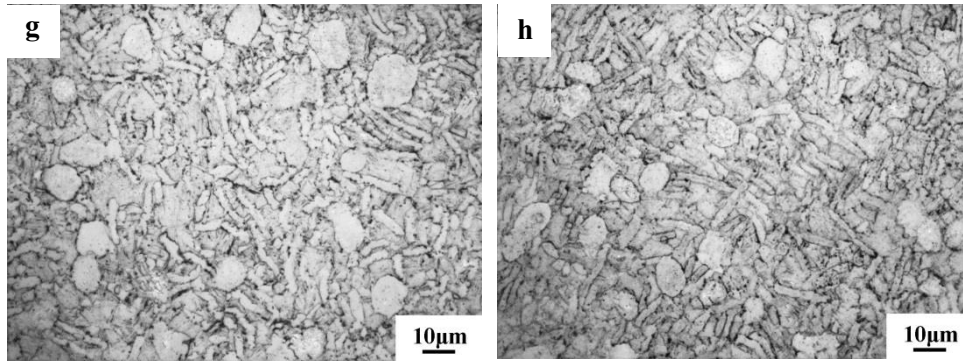


Fig. 22 The microstructure of CSP and MSP of parts at different IDTs: **a** T=855°C, CSP; **b** T=855°C, MSP; **c** T=885°C, CSP; **d** T=885°C, MSP; **e** T=915°C, CSP; **f** T=915°C, MSP; **g** T=945°C, CSP; **h** T=945°C, MSP

Conclusions

1. The surface steps of the parts are mainly caused by the elliptical deformation in the rolling process. With the increase of IDT, the elliptical deformation is serious, so there are obvious steps on the surface of the rolled parts after rolling at high temperatures. After several IDT experiments, the results showed that surface quality of the rolled workpiece is the best at 885 °C.
2. Compared with the CWR process at different IDTs, the lower the IDT is, the greater the radial force and torque are required. When the IDT is 945 °C, the radial force and torque are about 73 kN and 8 kN•m, respectively. When the IDT is 855 °C, the radial force and torque are about 106 kN and 11.5 kN•m, respectively, which are 1.4 times higher than those at 945 °C.
3. The die gap reduces the interaction time between the die and the workpiece and the number of alternating cycles of tensile-compression stress in the rolled workpiece, resulting in no internal defects in the TC4 alloy rolled workpiece in the high IDT range of 855-945 °C.
4. The mechanical properties of UTS, YS and EI of TC4 alloy were jointly affected by primary α phase content and microstructure morphology. The microstructure of the parts was refined after rolling, and the mechanical properties were improved compared with the initial state. At the IDT of 885 °C, the UTS, YS and EI were 987MPa, 924MPa and 16.8 %, respectively. It shows that the parts with high tensile strength and elongation can be obtained by hot CWR process, which can meet the requirements of the mechanical properties of the lower arm preform.

Acknowledgements

This work is supported by the National Key R&D Program of China (Grant No. 2018YFB1307900), and the National Natural Science Foundation of China (Grant No. 51875036)

Authors' contributions Peiai Li: conceptualization, investigation, methodology, data curation, writing-original draft, reviewing and editing.

Baoyu Wang: supervision, conceptualization, methodology, funding acquisition, reviewing and editing.

Pengni Feng: supervision, methodology, reviewing and editing.

Jinxia Shen: supervision, methodology, reviewing and editing.

Jiapeng Wang: supervision, methodology, reviewing and editing.

447 **Data availability** The datasets generated and/or analysed during the current study are
448 available from the corresponding author on reasonable request.

449

450

451 **Conflicts of interest** The authors have no conflicts of interest to declare that are relevant to
452 the content of this article.

453

454 **Ethical approval** The article follows the guidelines of the Committee on Publication Ethics
455 (COPE) and involves no studies on human or animal subjects.

456

457 **Consent to participate** Applicable.

458 **Consent to publish** Applicable.

459

460 **References**

461 [1] Boyer RR (1996) An overview on the use of titanium in the aerospace industry. *Mater Sci Eng A*
462 213(1-2):103-114. [https://doi.org/10.1016/0921-5093\(96\)10233-1](https://doi.org/10.1016/0921-5093(96)10233-1)

463 [2] Leyens C, Peters M (2003) Titanium and titanium alloys: fundamentals and applications. *Publ*
464 *House Wiley-VCH* 38(6):401.

465 [3] Poondla N, Srivatsan TS, Patnaik A, Petraroli M (2009) A study of the microstructure and
466 hardness of two titanium alloys: commercially pure and Ti-6Al-4V. *J Alloy Compd*
467 486(1-2):162-167. <https://doi.org/10.1016/j.jallcom.2009.06.172>

468 [4] Arrazola PJ, Garay A, Lriarte LM, Armendia M, Marya S, Maître FL (2009) Machinability of
469 titanium alloys (Ti6Al4V and Ti555.3). *J Mater Process Tech* 209(5):2223-2230.
470 <https://doi.org/10.1016/j.jmatprotec.2008.06.020>

471 [5] Guo P, Zhao YQ, Zeng WD, Hong Q (2013) The effect of microstructure on the mechanical
472 properties of TC4-DT titanium alloys. *Mater Sci Eng A* 563(2):106-111.
473 <https://doi.org/10.1016/j.msea.2012.11.033>

474 [6] Li JL, Wang BY, Fang S, Chen P (2020) A new process chain combining cross-wedge rolling and
475 isothermal forging for the forming of titanium alloy turbine blades. *Int J Adv Manuf Tech*
476 108(5-6):1827-1838.

477 [7] Hu ZH, Zhang KS, Wang BY, Shu XD, Yang CP (2004) Forming technology and simulation of
478 cross wedge rolling parts. *Metall Ind Press, Beijing* (in Chinese)

479 [8] Ji HC, Liu JP, Wang BY, Zheng ZH, Huang JH, Hu ZH (2015) Cross-wedge rolling of a 4Cr9Si2
480 hollow valve: explorative experiment and finite element simulation. *Int J Adv Manuf Tech*
481 77(1-4):15-26. <https://doi.org/10.1007/s00170-014-6363-9>

482 [9] Ji HC, Liu JP, Wang BY, Zhang ZR, Zhang T, Hu ZH (2015) Numerical analysis and experiment
483 on cross wedge rolling and forging for engine valves. *J Mater Process Tech* 221:233-242.
484 <https://doi.org/10.1016/j.jmatprotec.2015.02.007>

485 [10] Li Q, Lovell MR, Slaughter W, Tagavi K (2002) Investigation of the morphology of internal
486 defects in cross wedge rolling. *J Mater Process Tech* 125-126(3):248-257.
487 [https://doi.org/10.1016/S0924-0136\(02\)00303-5](https://doi.org/10.1016/S0924-0136(02)00303-5)

488 [11] Jia Z, Zhou J, Ji JJ, Lei ZZ, Xiang D, Sun XT (2013) Influence analysis of area reduction for
489 necking in twice-stage cross wedge rolling. *Int J Adv Manuf Tech.* 66(9-12):1407-1413.
490 <https://doi.org/10.1007/s00170-012-4418-3>

- 491 [12] Pater Z (1999) Numerical simulation of the cross wedge rolling process including upsetting. *J*
492 *Mater Process Tech* 92-93(0):468-473. [https://doi.org/10.1016/S0924-0136\(99\)00231-9](https://doi.org/10.1016/S0924-0136(99)00231-9)
- 493 [13] Pater Z (2000) Theoretical and experimental analysis of cross wedge rolling process. *Int J Mach*
494 *Tool Manu* 40(1):49-63. [https://doi.org/10.1016/S0890-6955\(99\)00047-4](https://doi.org/10.1016/S0890-6955(99)00047-4)
- 495 [14] Pater Z (2006) Finite element analysis of cross wedge rolling. *J Mater Process Tech*
496 173(2):201-208. <https://doi.org/10.1016/j.jmatprotec.2005.11.027>
- 497 [15] Maraghechi H, Rajabipour F, Pantano CG, Burgos WD (2018) Micro-mechanism of central
498 damage formation during cross wedge rolling. *J Mater Process Technol* 252:322-332.
499 <https://doi.org/10.1016/j.jmatprotec.2017.09.041>
- 500 [16] Lee HW, Lee GA, Yoon DJ, Choi S, Na KH, Hwang MY (2008) Optimization of design
501 parameters using a response surface method in a cold cross-wedge rolling. *J Mater Process Tech*
502 201(1-3):112-117. <https://doi.org/10.1016/j.jmatprotec.2007.11.287>
- 503 [17] Li JG, Liu JP, Hu ZH (2008) Study on influencing factors of torsional deflection in cross wedge
504 rolling. *Forg Stamping Technology* 33(4):67-71. (in Chinese)
- 505 [18] Shu XD, Nie GZ, Li LP (2007) Study on Influence of die void on rolling force during cross wedge
506 rolling. *Chin Metall* 17(7):38-40. (in Chinese)
- 507 [19] Pater Z, Bulzak T, Tomczak J (2016) Cross-wedge rolling of driving shaft from titanium alloy
508 Ti6Al4V. *Key Eng Mater* 687:125-132. <https://doi.org/10.4028/www.scientific.net/KEM.687.125>
- 509 [20] Çakırcalı M, Kılıçaslan C, Güden M, Kıranlı E, Shchukin VY, Petronko VV (2013) Cross wedge
510 rolling of a Ti6Al4V (ELI) alloy: the experimental studies and the finite element simulation of the
511 deformation and failure. *Int J Adv Manuf Tech* 65(9-12):1273-1287.
512 <https://doi.org/10.1007/s00170-012-4256-3>
- 513 [21] Huang X, Wang BY, Mu YH, Shen JX, Li JL, Zhou J (2019) Investigation on the effect of
514 mandrels on hollow shafts in cross-wedge rolling. *Int J Adv Manuf Tech* 102(1-4):443-455.
515 <https://doi.org/10.1007/s00170-018-3093-4>
- 516 [22] Ji HC, Dong JW, Xin L, Huang XM, Liu JP (2018) Numerical and experimental study on the
517 thermodynamic coupling of Ti-6Al-4V blade preforms by cross wedge rolling. *Metals* 8(12):1054.
518 <https://doi.org/10.3390/met8121054>
- 519 [23] Li JL, Wang BY, Ji HC, Huang X, Tang XF, Ma WP (2017) Effects of the cross-wedge rolling
520 parameters on the formability of Ti-6Al-4V alloy. *Int J Adv Manuf Tech* 92(5-8):2217-2229.
521 <https://doi.org/10.1007/s00170-017-0263-8>
- 522 [24] Shi ZF, Guo HZ, Liu R, Wang XC, Yao ZK (2015) Microstructure and mechanical properties of
523 TC21 titanium alloy by near-isothermal forging. *Trans Nonferr Met Soc* 25(1):72-79.
524 [https://doi.org/10.1016/S1003-6326\(15\)63580-4](https://doi.org/10.1016/S1003-6326(15)63580-4)
- 525 [25] Zhang ZX, Qu SJ, Feng AH, Hu X, Shen J (2019) Microstructural mechanisms during
526 multidirectional isothermal forging of as-cast Ti-6Al-4V alloy with an initial lamellar
527 microstructure. *J Alloy Compd* 773:277-87. <https://doi.org/10.1016/j.jallcom.2018.09.220>
- 528 [26] Zhai DJ, Shui Y, Yuan M, Zhang YY, He YB (2019) Effects of content and morphology of α phase
529 on microstructure and mechanical properties of TC4 alloy. *Heat Treat Met* 44(10):129-134. (in
530 Chinese)
- 531 [27] Wang M, Yang H, Zhang C, Guo LG (2013) Microstructure evolution modeling of titanium alloy
532 large ring in hot ring rolling. *Int J Adv Manuf Tech* 66(9-12):1427-1437.
533 <https://doi.org/10.1007/s00170-012-4420-9>
- 534 [28] Li JL, Wang BY, Qin Y, Fang S, Huang X, Chen P (2019) Investigating the effects of process

- 535 parameters on the cross wedge rolling of TC6 alloy based on temperature and strain rate
536 sensitivities. Int J Adv Manuf Tech 103(5-8):2563-2577.
537 <https://doi.org/10.1007/s00170-019-03461-3>
- 538 [29] Peng XN, Guo HZ, Shi ZF (2013) Constitutive equations for high temperature flow stress of
539 TC4-DT alloy incorporating strain, strain rate and temperature. Mater Design 50(17):198-206.
540 <https://doi.org/10.1016/j.matdes.2013.03.009>
- 541 [30] Huang X, Wang BY, Zhou J, Ji HC, Mu YH, Li JL (2017) Comparative study of warm and hot
542 cross-wedge rolling: numerical simulation and experimental trial. Int J Adv Manuf Tech
543 92(9-12):3541-3551. <https://doi.org/10.1007/s00170-017-0399-6>
- 544 [31] Ren L, Xiao W, Chang H, Zhao Y, Ma C, Zhou L (2018) Microstructural tailoring and mechanical
545 properties of a multi-alloyed near β titanium alloy Ti-5321 with various heat treatment. Mater Sci
546 Eng: A 711:553-561. <https://doi.org/10.1016/j.msea.2017.11.029>

Figures

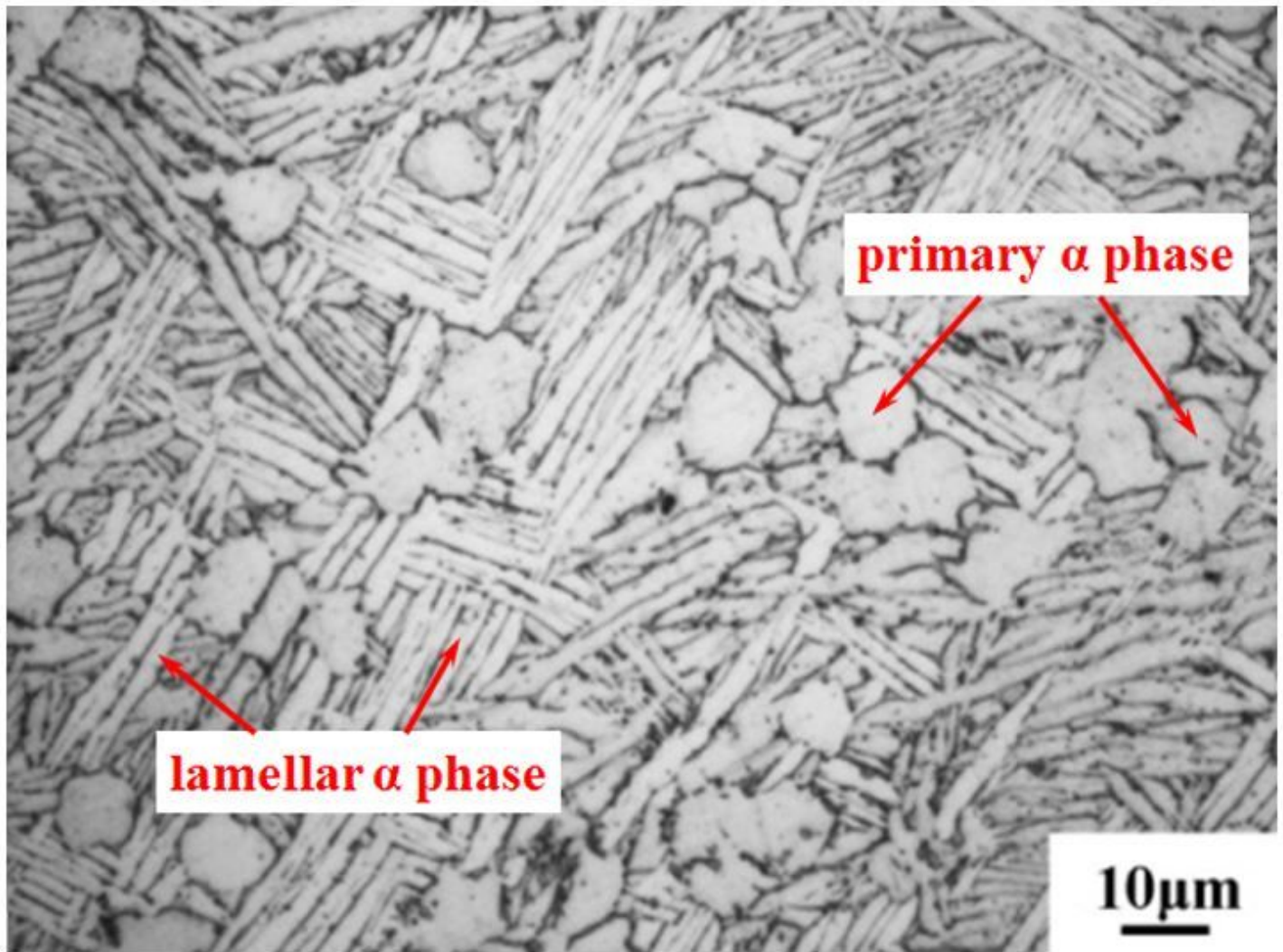


Figure 1

Optical micrograph of received TC4 alloy

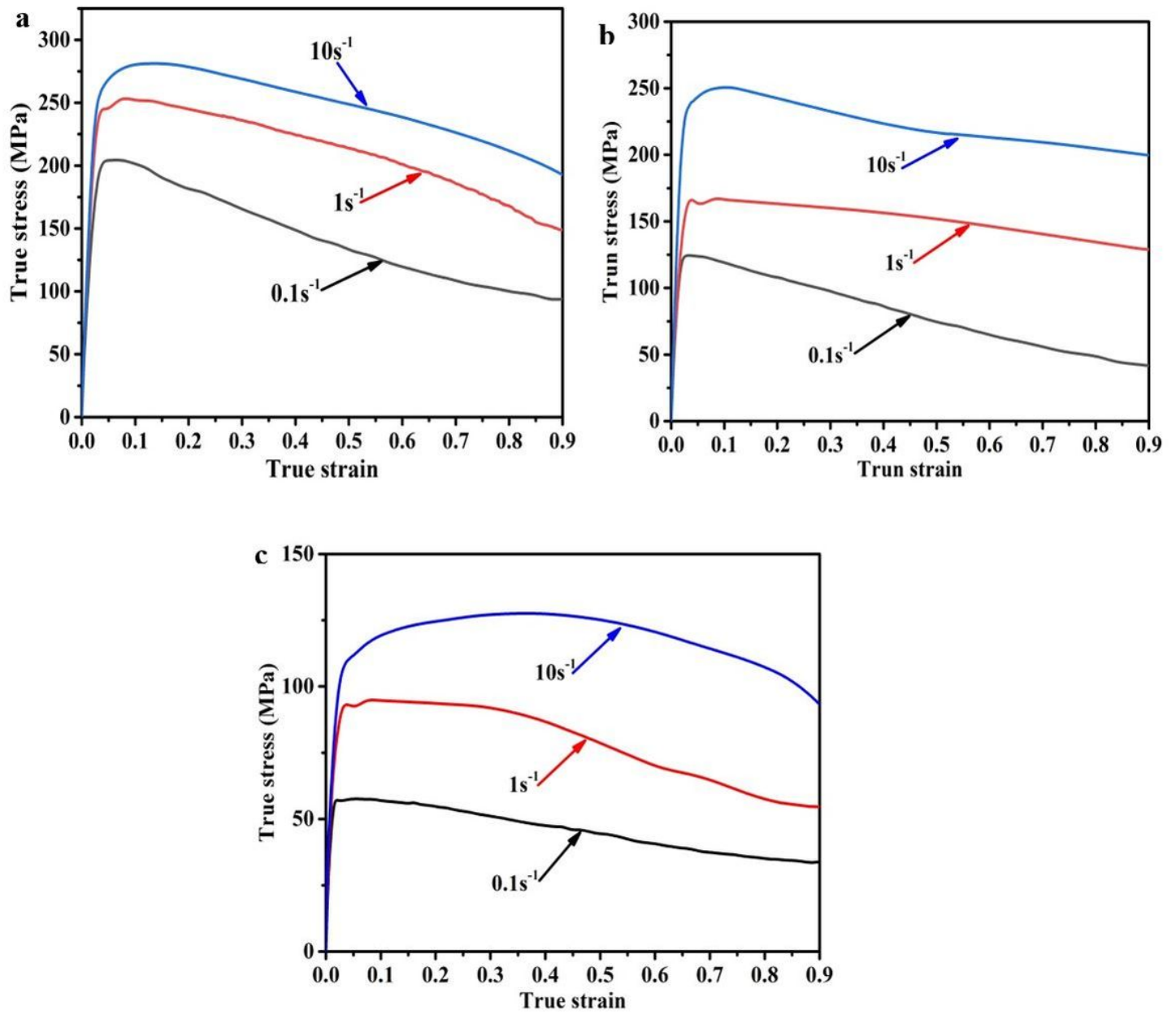


Figure 2

True stress-strain curves of TC4 alloy: a 850 °C, b 900 °C, c 950 °C

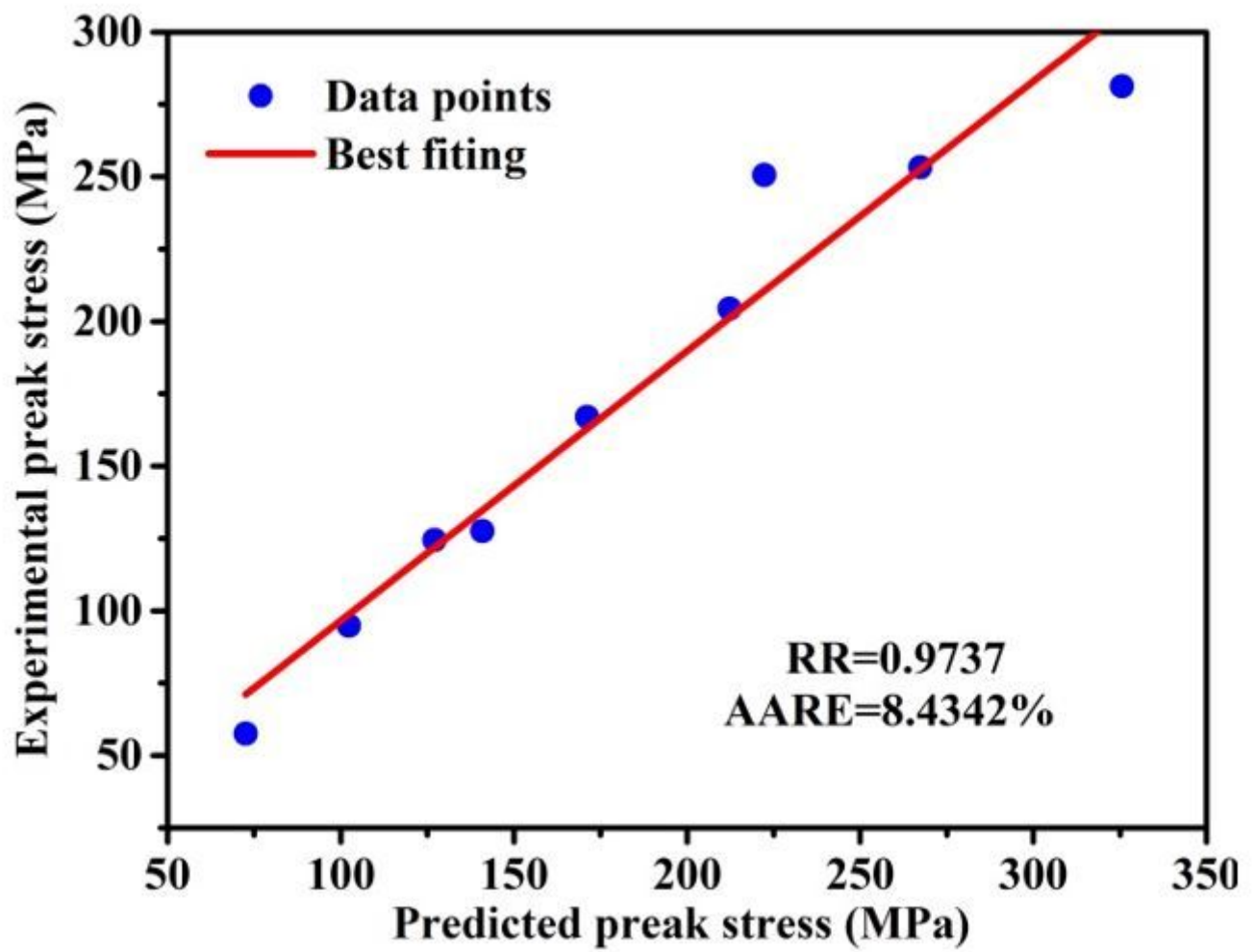


Figure 3

Comparison of predicted peak stress and experimental peak stress

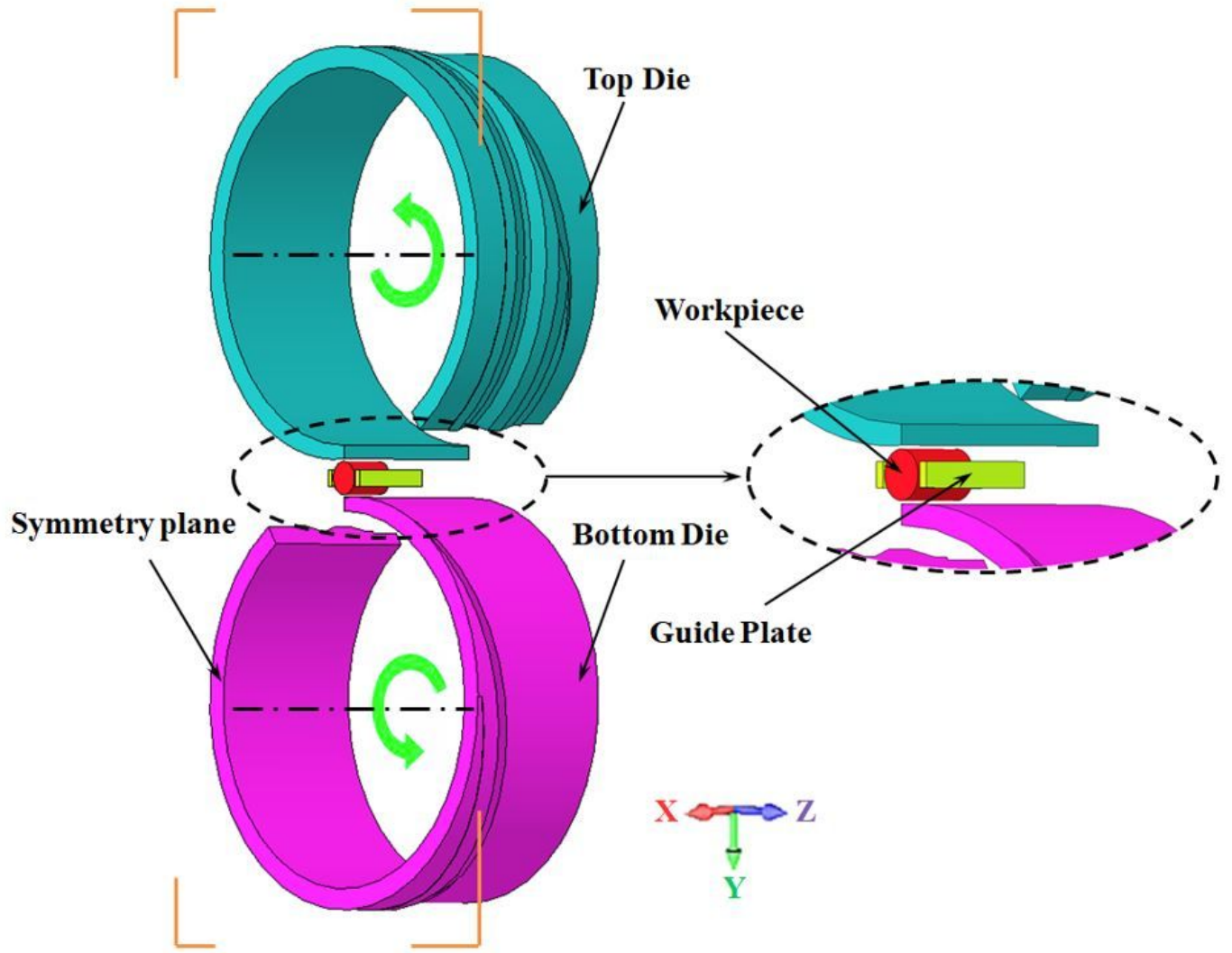


Figure 4

FEM of CWR for TC4 alloy

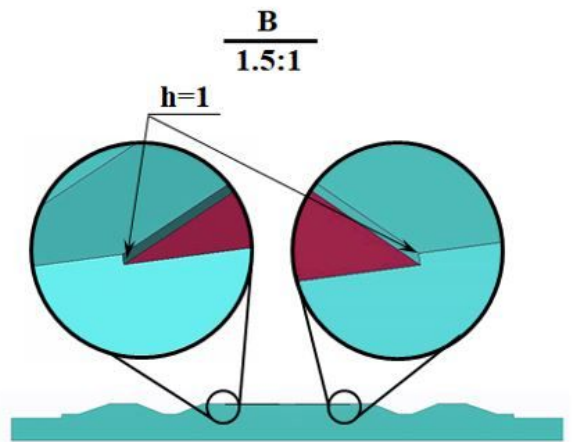
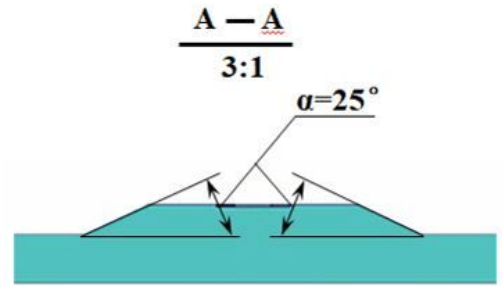
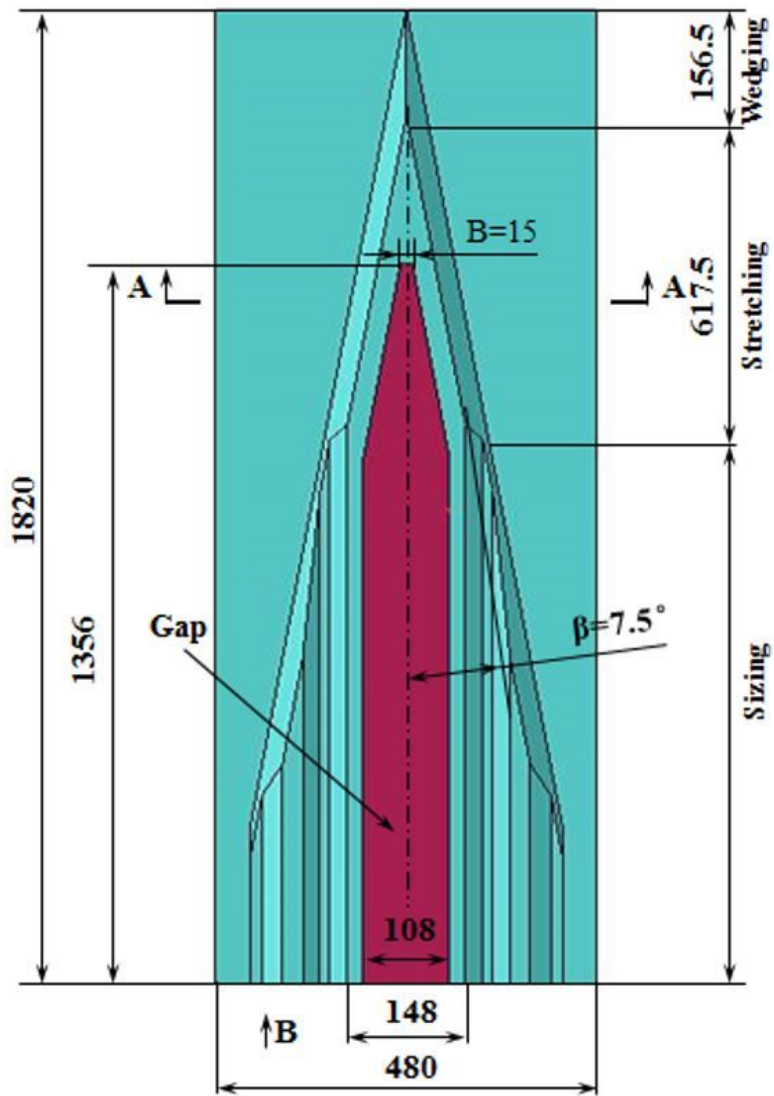


Figure 5

Forming wedge tool parameters for H630 rolling mill



Figure 6

Experimental equipment and manufactured die: a H630 mill, b Forming wedge dies



Figure 7

The parts of rolled

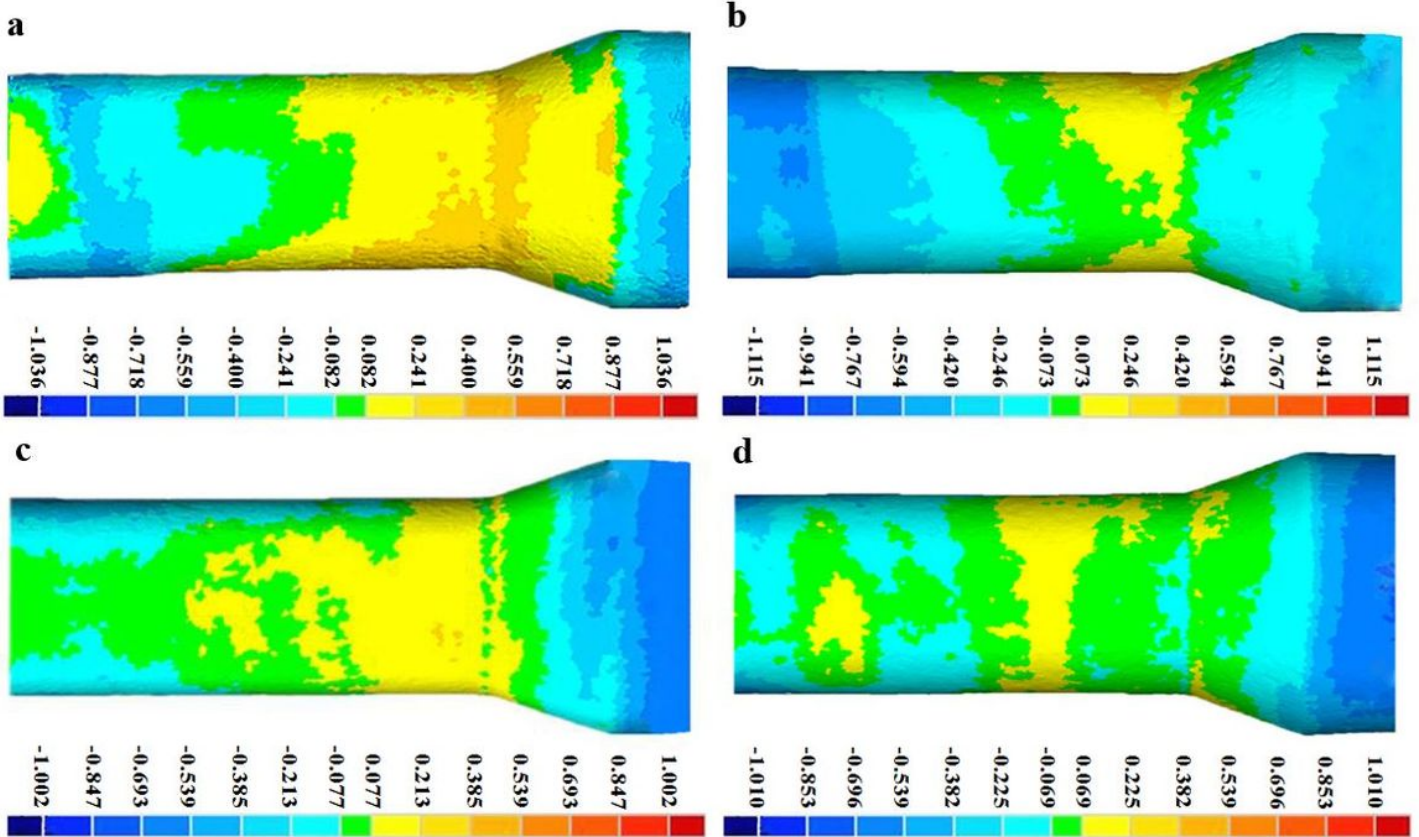


Figure 8

Comparison of TC4 Alloy CWR Parts and simulated results: a IDT at 945°C, b IDT at 915°C, c IDT at 885°C, d IDT at 855°C

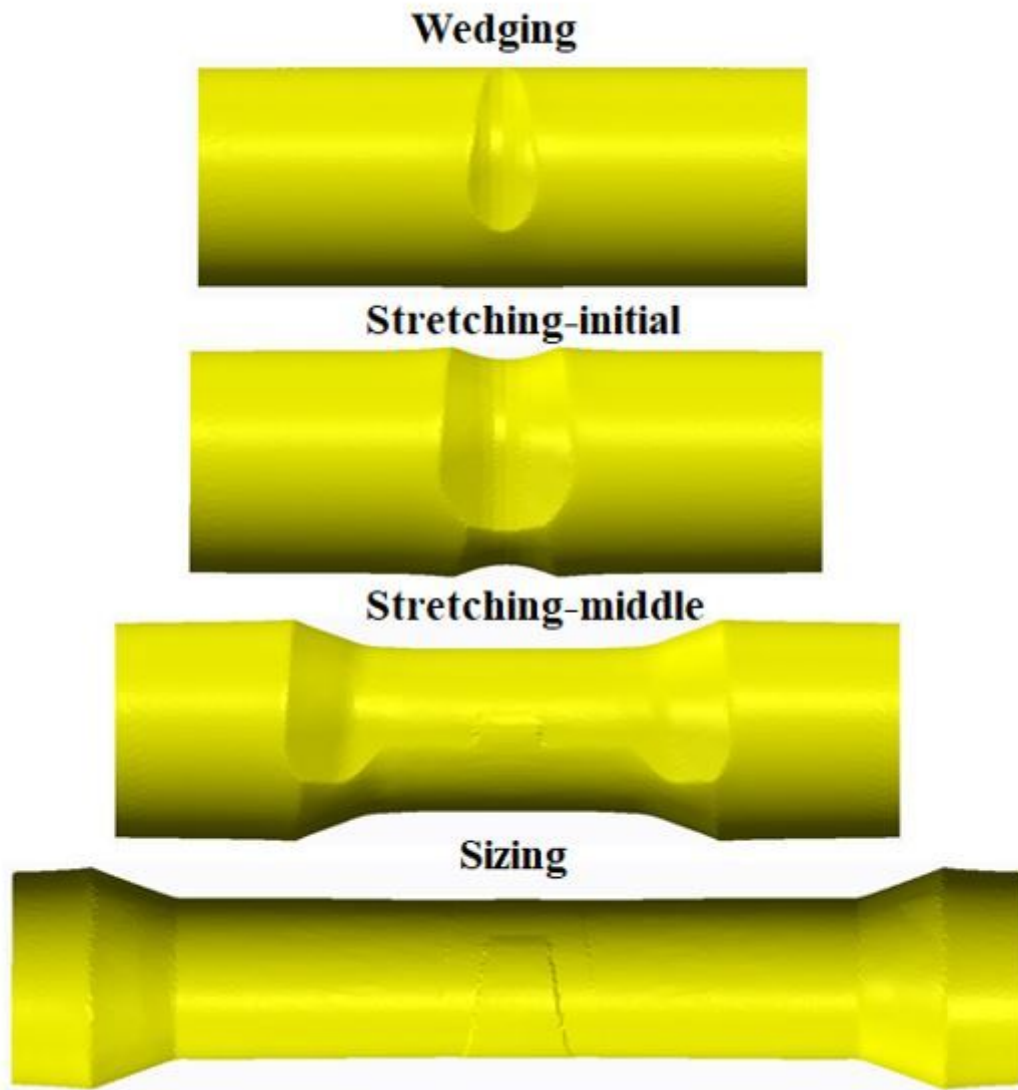


Figure 9

Different stages of CWR and step forming

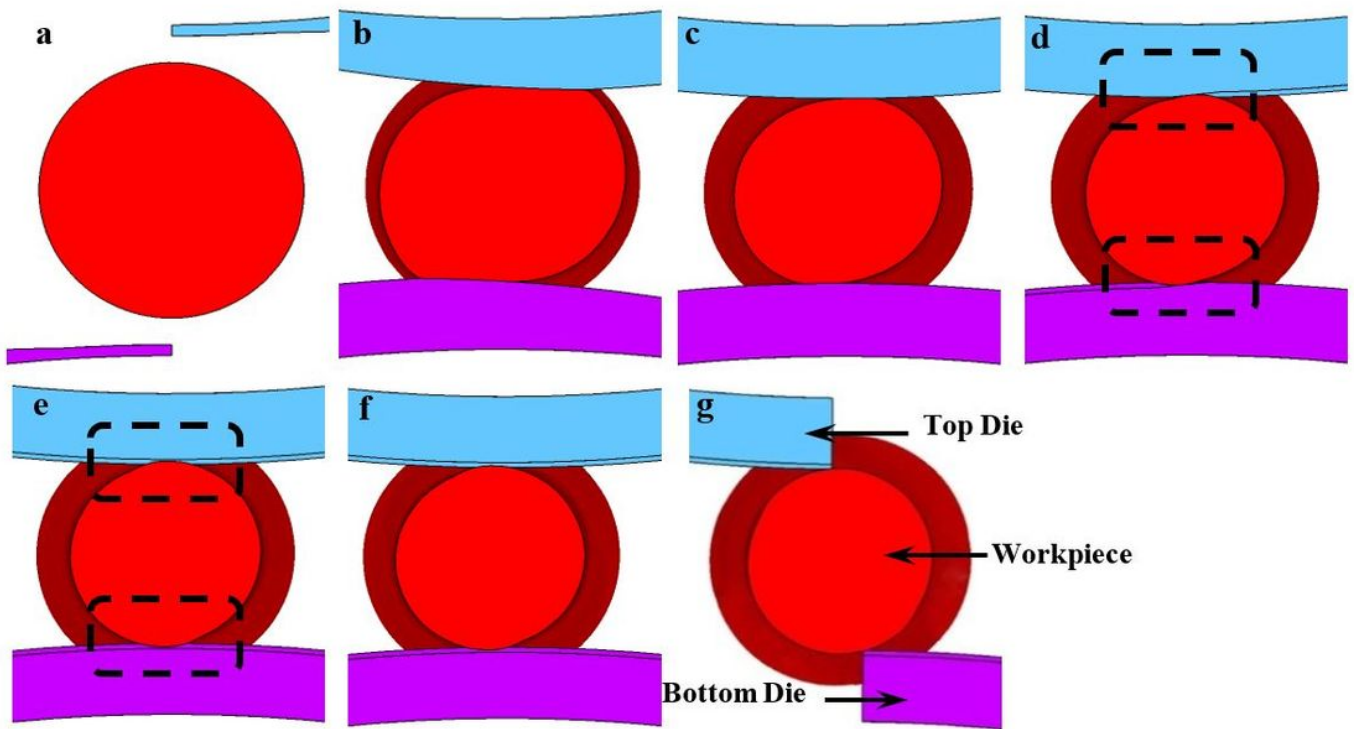


Figure 10

Cross-section profile during forming process at IDT of 945 °C: a initial status $t=0s$, b wedging stage $t=0.8s$, c stretching stage $t=1.52s$, d preparing for the gap stage $t=1.84s$, e gap stage $t=2.4s$, f sizing stage $t=3.2s$, g completion status $t=5.64s$

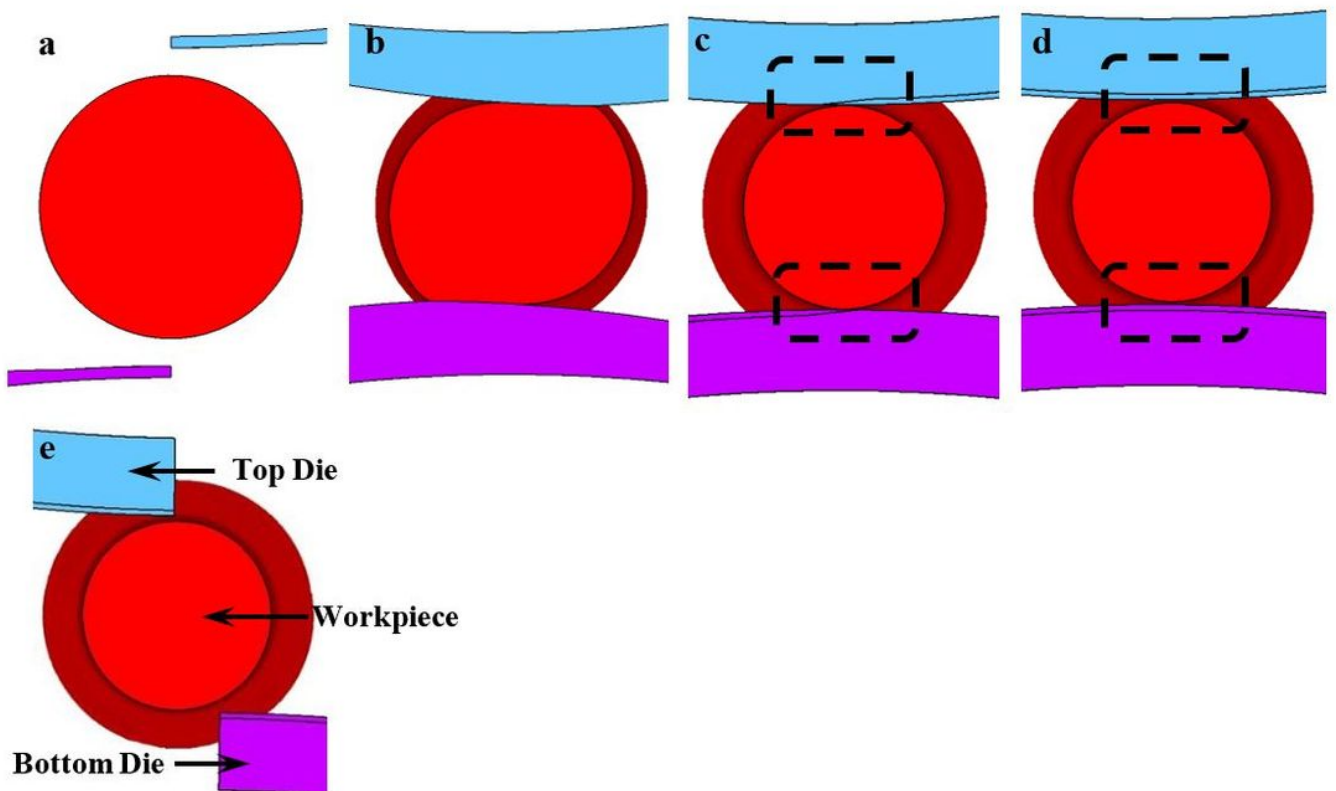


Figure 11

Cross-section profile during forming process at IDT of 885 °C: a initial status $t=0s$, b wedging stage $t=0.8s$, c preparing for the gap stage $t=1.84s$, d sizing stage $t=3.2s$, e completion status $t=5.64s$

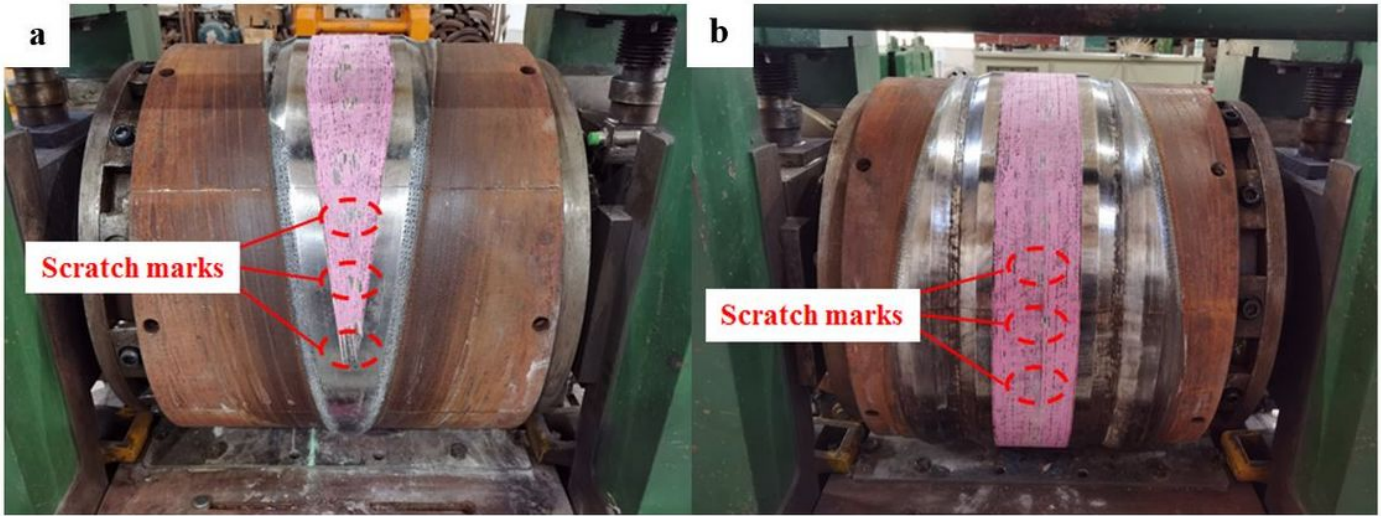


Figure 12

The distribution of scratch marks on the surface of the die gap area: a scratch marks in stretching zone, b scratch marks in sizing zone

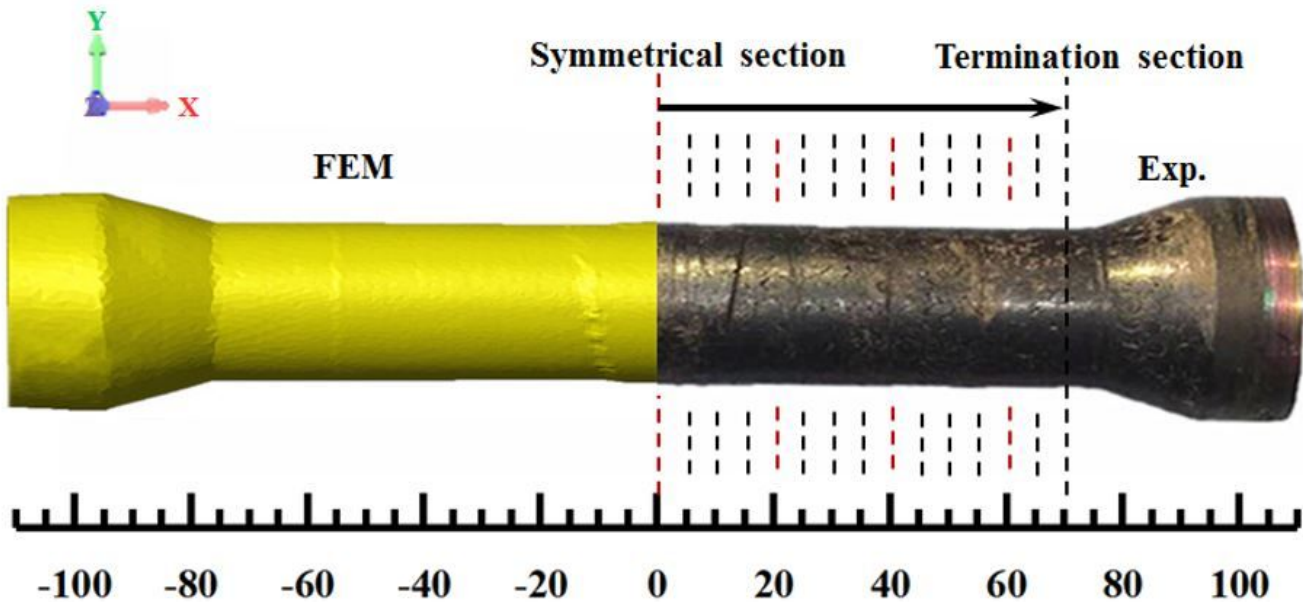


Figure 13

Cross-section distribution position

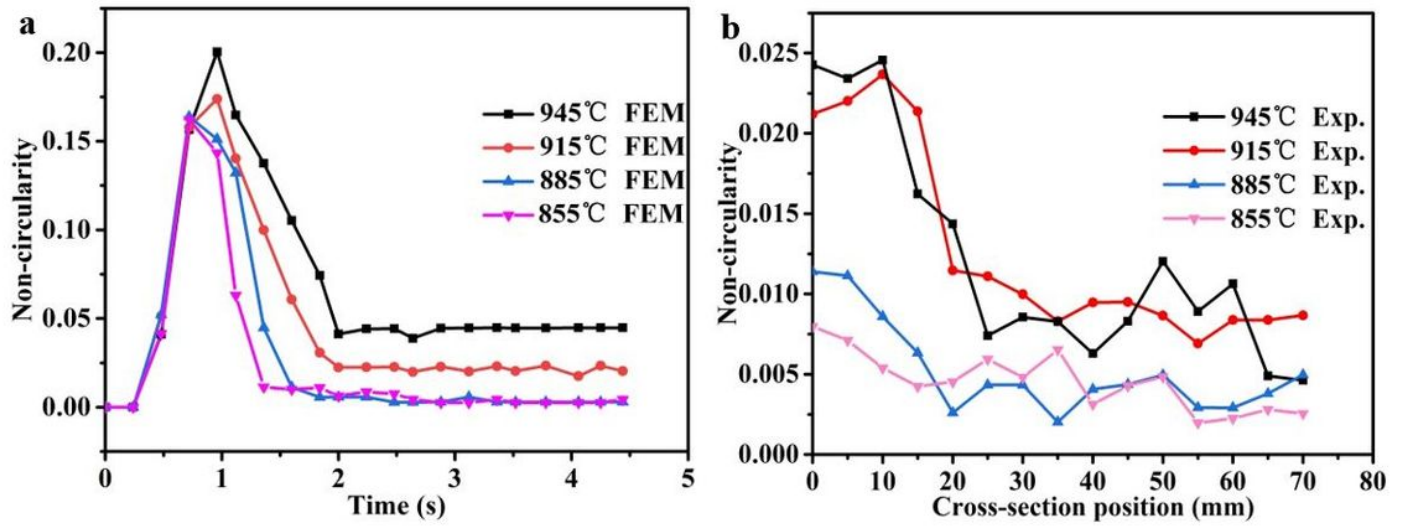


Figure 14

Non-circularity value of outer surface of parts at different IDT: a non-circularity results of symmetric section of FEM during rolling, b non-circularity results of experiments at different axial position

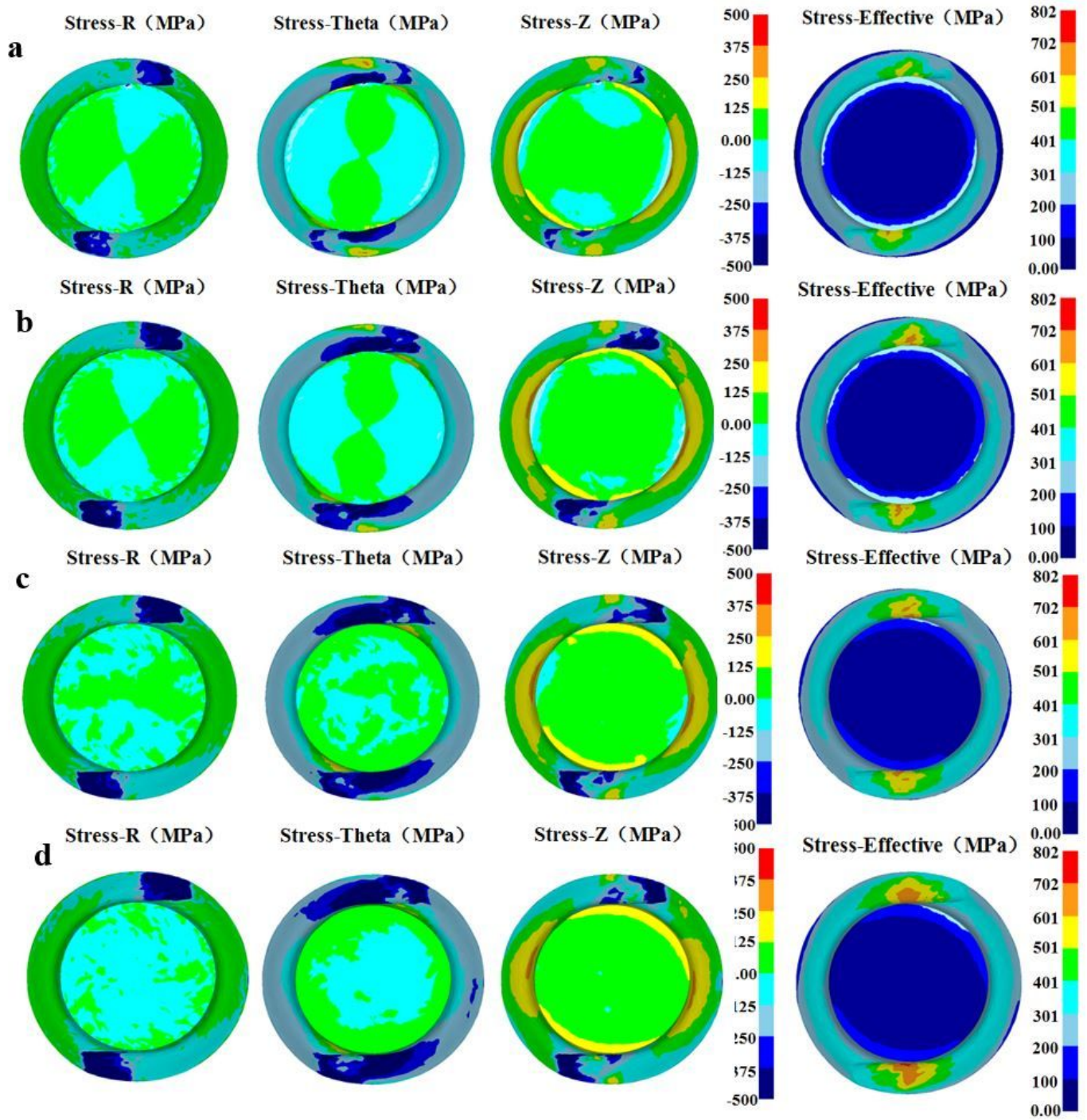


Figure 15

Stress distribution in the stretching zone: a $T=945\text{ }^{\circ}\text{C}$, b $T=915\text{ }^{\circ}\text{C}$, c $T=885\text{ }^{\circ}\text{C}$, d $T=855\text{ }^{\circ}\text{C}$

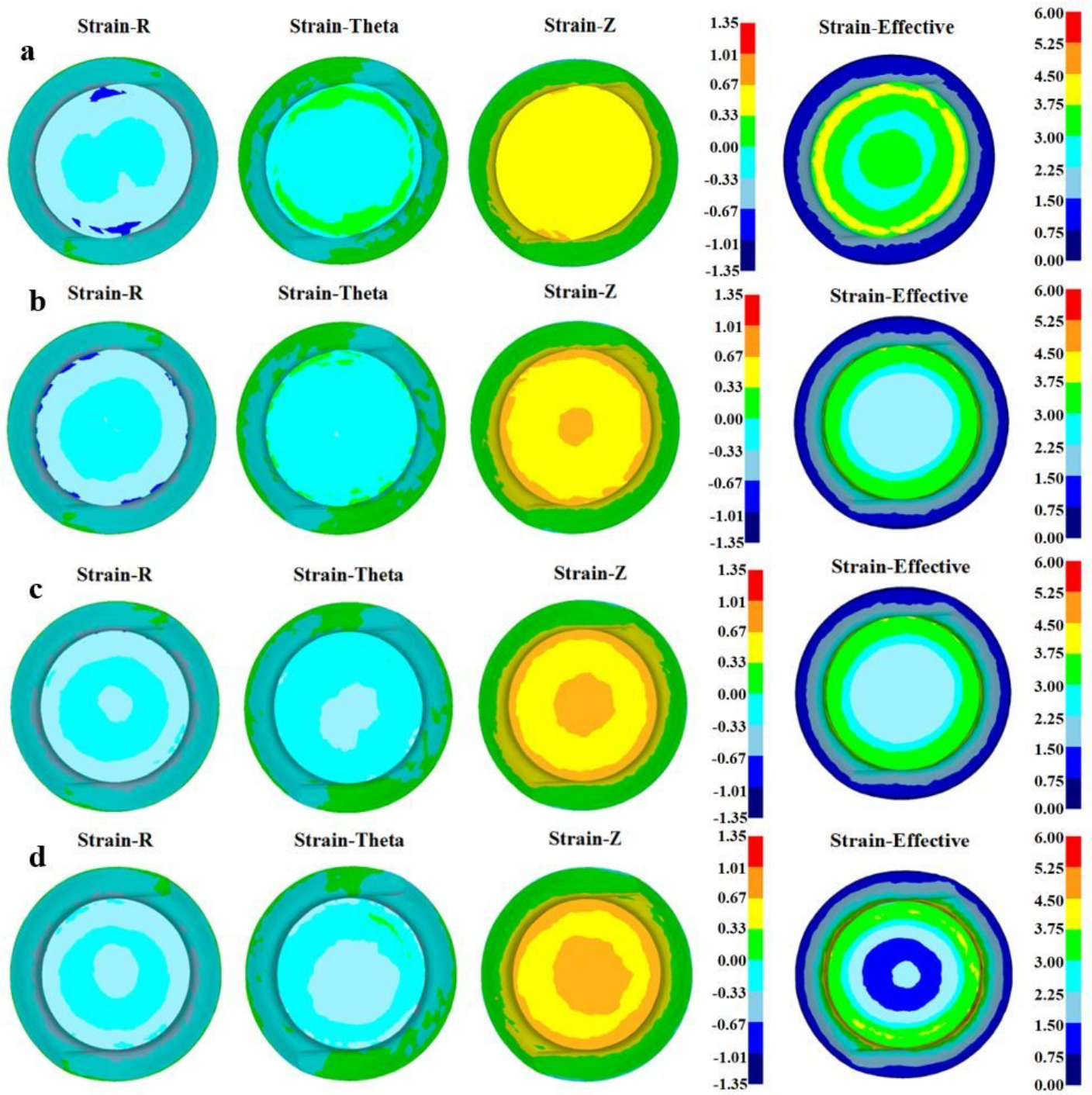


Figure 16

Strain distribution in the stretching zone: a $T = 945\text{ }^{\circ}\text{C}$, b $T = 915\text{ }^{\circ}\text{C}$, c $T = 885\text{ }^{\circ}\text{C}$, d $T = 855\text{ }^{\circ}\text{C}$

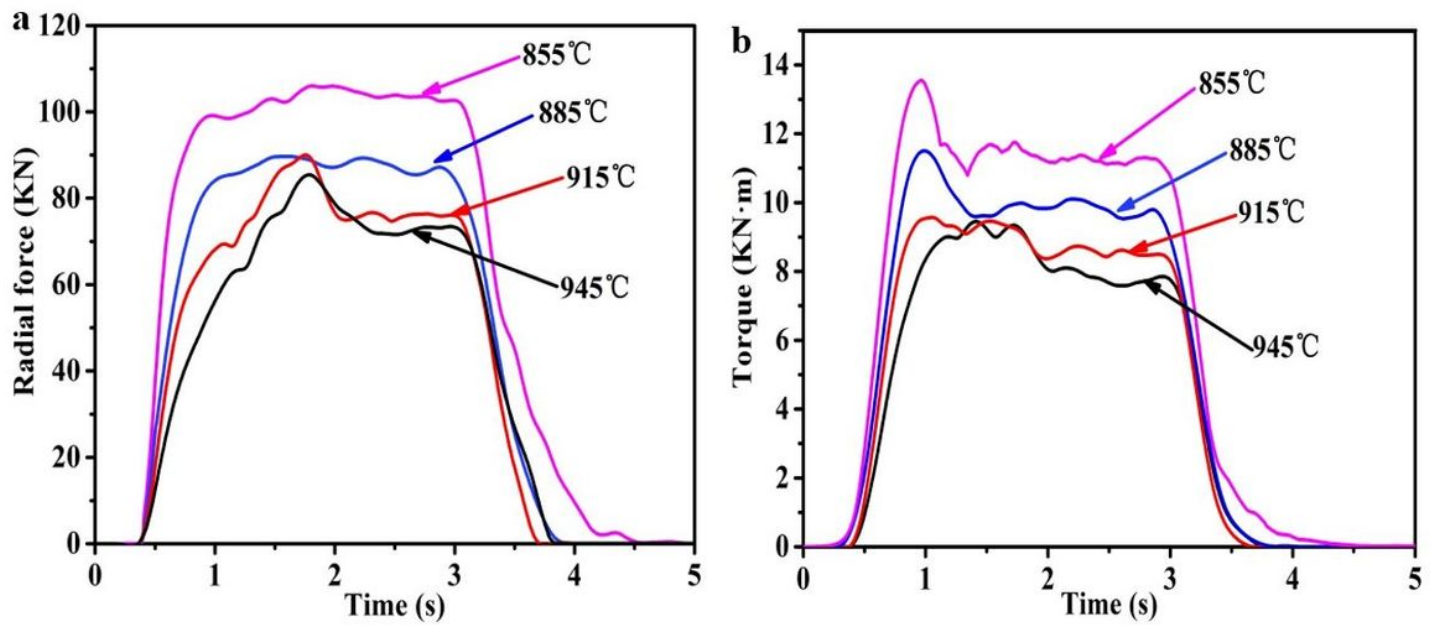


Figure 17

Effective of the IDTs on force and torque in CWR processes

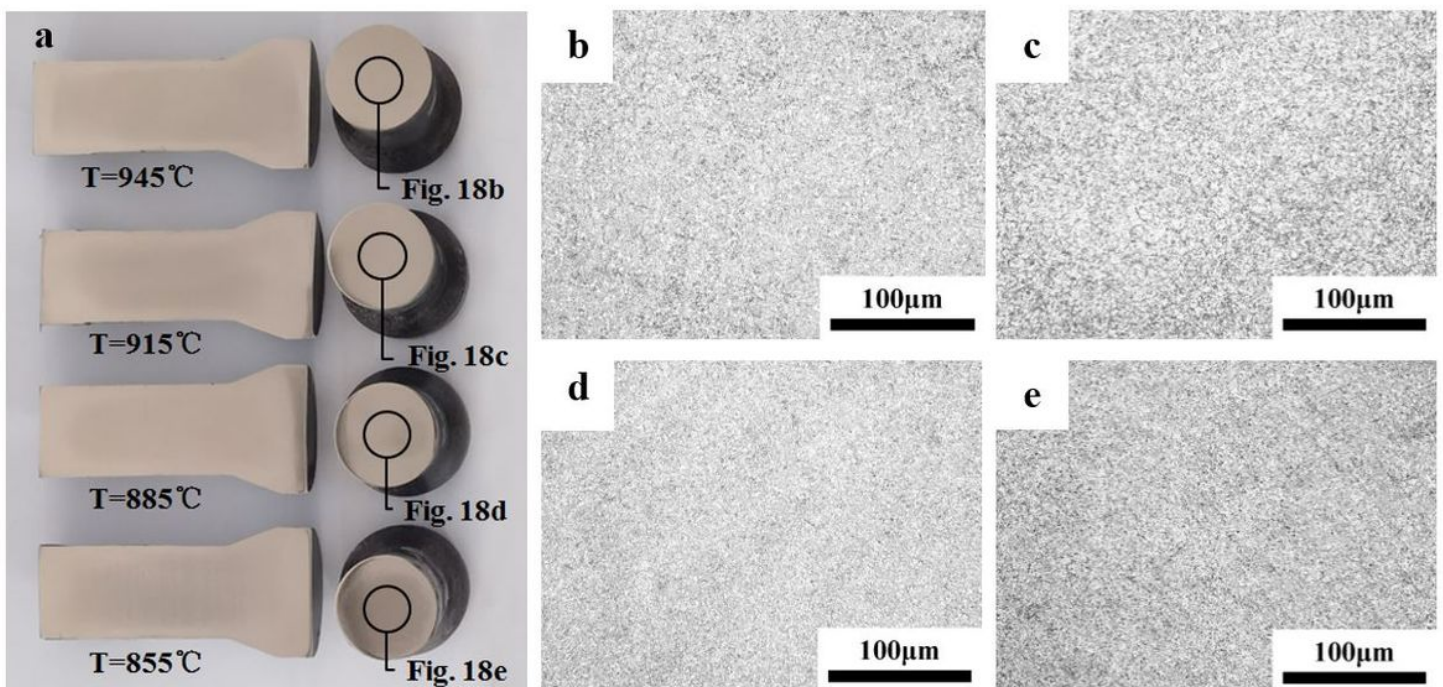


Figure 18

Internal quality of parts at different IDTs: a sectional display of different parts, b T=945 °C, c T=915 °C, d T=885 °C, e T=855 °C

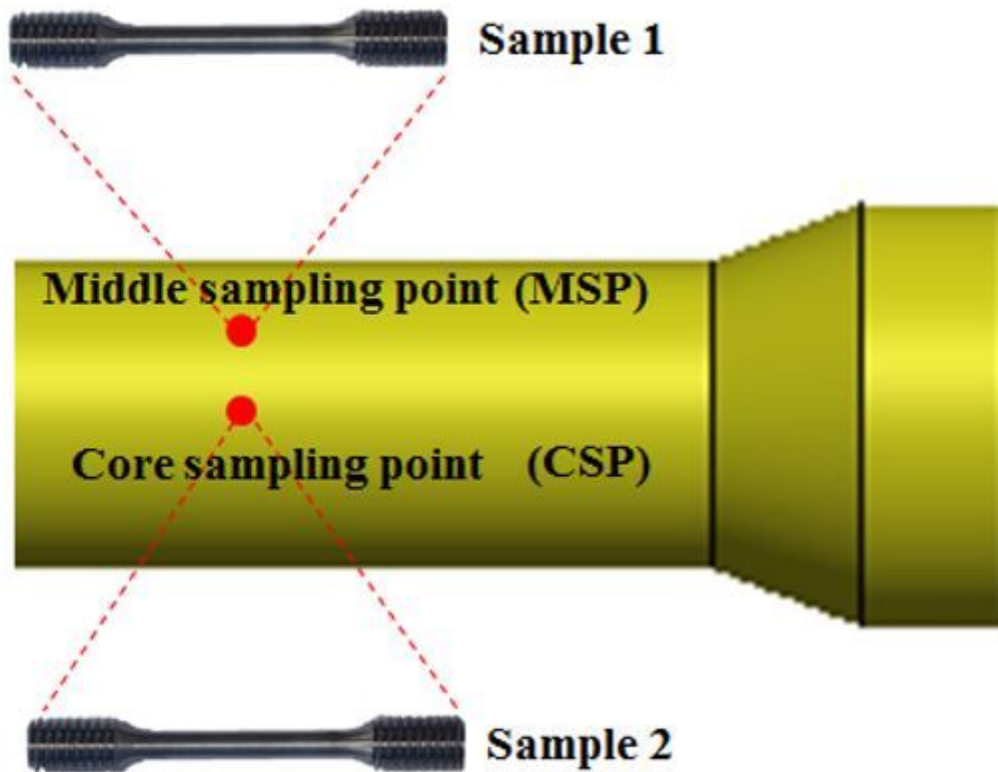


Figure 19

Mechanical properties and microstructure test sampling position distribution

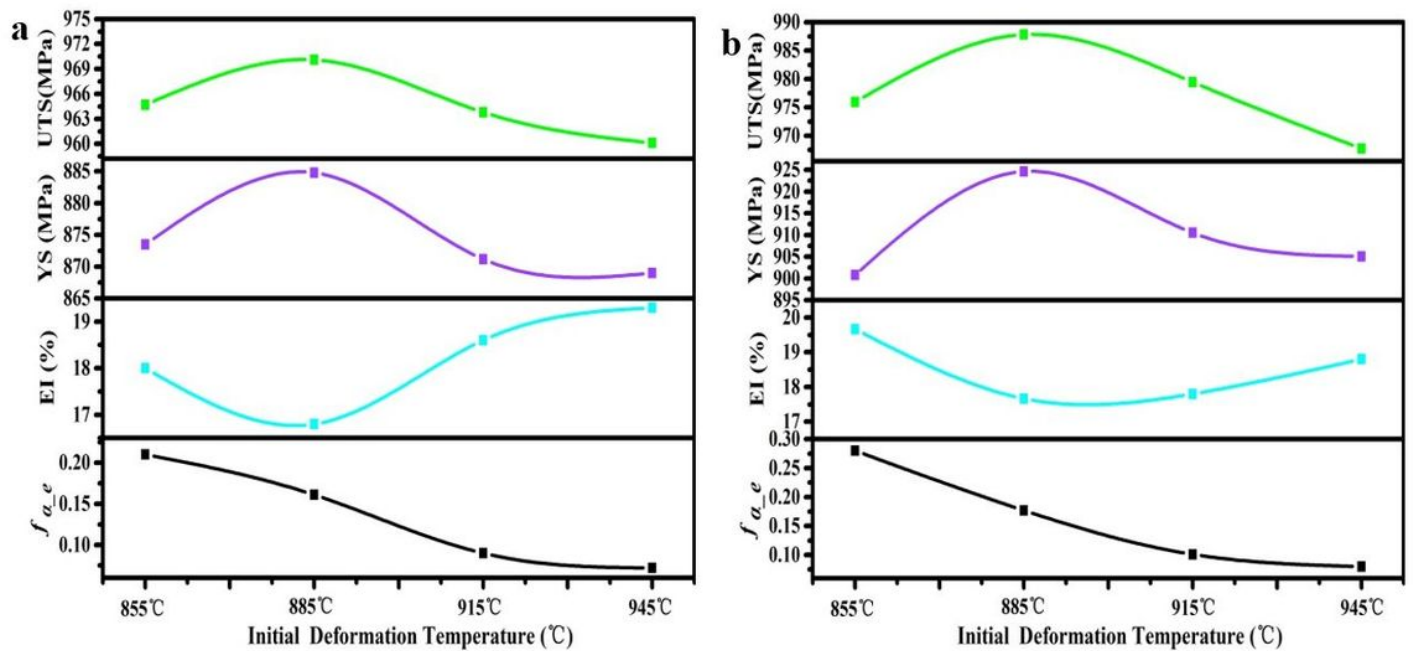


Figure 20

Comparison of the mechanical properties at different IDTs of a CSP b MSP

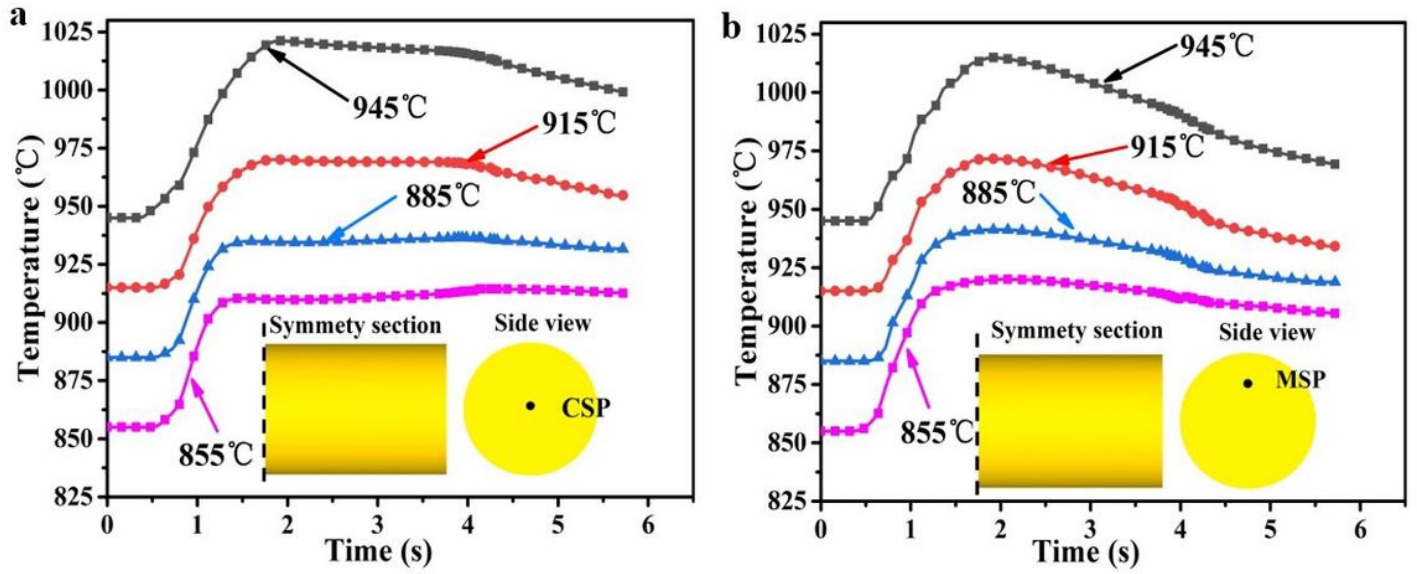


Figure 21

Temperature distribution of CWR forming TC4 alloy in symmetry sections: a CSP, b MSP

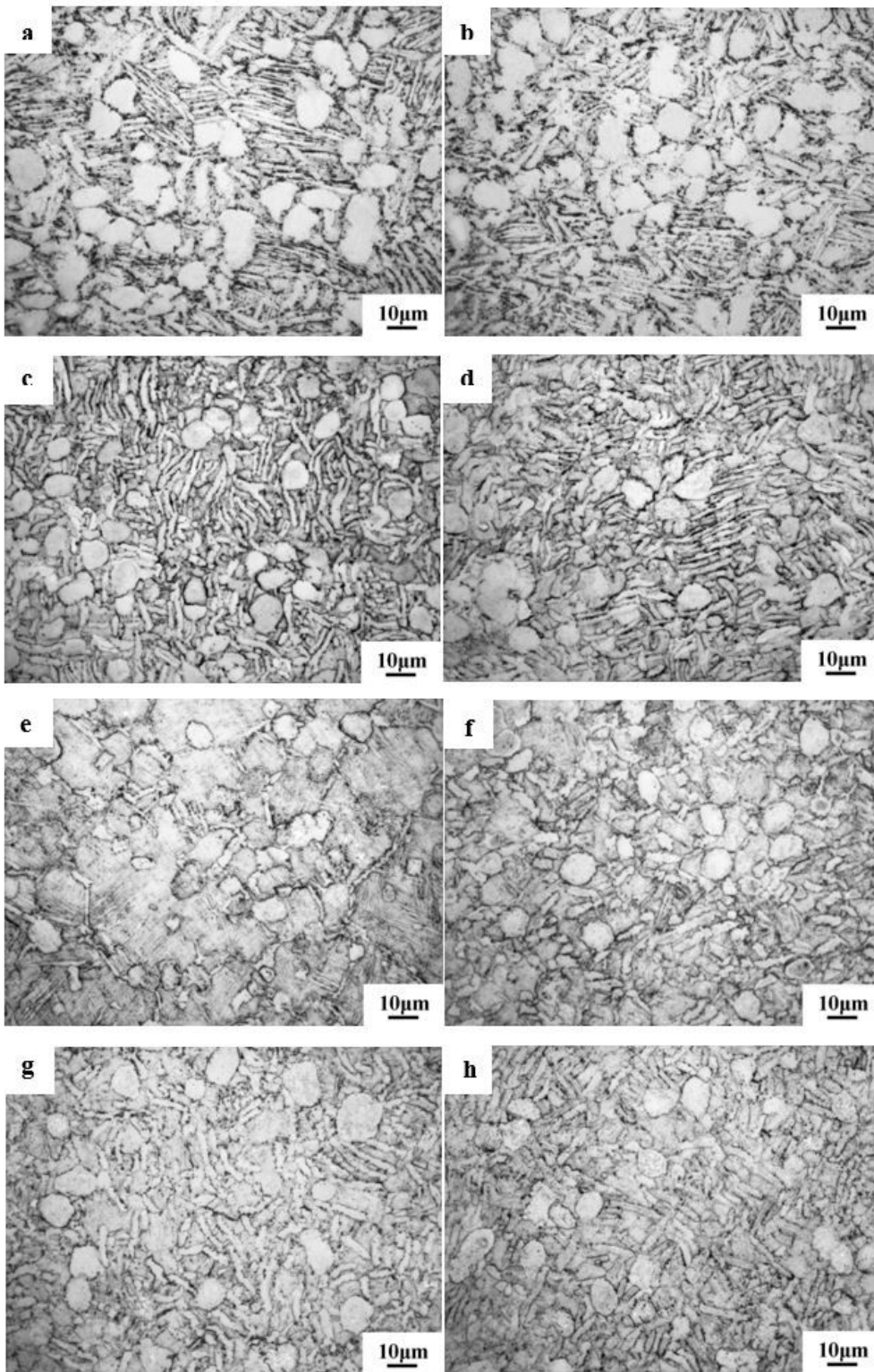


Figure 22

The microstructure of CSP and MSP of parts at different IDTs: a T=855°C, CSP; b T=855°C, MSP; c T=885°C, CSP; d T=885°C, MSP; (e) T=915°C, CSP; f T=915°C, MSP; g T=945°C, CSP; h T=945°C, MSP